

AD A 055060

FOR FURTHER TRAN

ARO 14653.5-R-EL

5
act

RADAR IMAGE MODELING AND PROCESSING FOR REAL-TIME RF SIMULATION

FINAL REPORT

ARO GRANT No. DAAG2977G0044

Nov. 20, 1976 - Feb. 19, 1978

Anil K. Jain
Jaswant R. Jain

DDC
RECEIVED
JUN 14 1978
B

Department of Electrical Engineering
State University of New York at Buffalo
223 Bell Hall
Amherst, N.Y. 14260

DISTRIBUTION STATEMENT A

Approved for public release;
Distribution Unlimited

AD No. _____
DDC FILE COPY

REPORT DOCUMENTATION PAGE		READ INSTRUCTIONS BEFORE COMPLETING FORM
1. REPORT NUMBER <u>AR3 74053, 5-R-EL</u> <u>AVJ-ARO-78</u>	2. GOVT ACCESSION NO.	3. RECIPIENT'S CATALOG NUMBER
4. TITLE (and Subtitle) <u>RADAR IMAGE MODELING AND PROCESSING FOR REAL-TIME RF SIMULATION.</u>		5. TYPE OF REPORT & PERIOD COVERED <u>Final Report, 20 Nov 76 - 11/20/76-2/19/78 - 19 Feb 78</u>
6. PERFORMING ORG. REPORT NUMBER <u>AVJ-ARO-78</u>		7. CONTRACT OR GRANT NUMBER(s) <u>ARO Grant No. DAAG2977G0044 New</u>
8. AUTHOR(s) <u>Anil K./Jain</u> <u>Jaswant R./Jain</u>		9. PERFORMING ORGANIZATION NAME AND ADDRESS <u>SUNYAB</u> <u>Dept. of Electrical Engineering, Bell Hall Rm223</u> <u>Amherst, NY 14260</u>
10. CONTROLLING OFFICE NAME AND ADDRESS <u>U. S. Army Research Office</u> <u>Post Office Box 12211</u> <u>Research Triangle Park, NC 27709</u>		11. REPORT DATE <u>15 Mar 1978</u>
12. MONITORING AGENCY NAME & ADDRESS (if different from Controlling Office)		13. NUMBER OF PAGES <u>57</u> <u>(1264 P.)</u>
14. DISTRIBUTION STATEMENT (of this Report) <u>Approved for public release; distribution unlimited.</u>		15. SECURITY CLASS. (of this report) <u>Unclassified</u>
16. DISTRIBUTION STATEMENT (of the abstract entered in Block 20, if different from Report) <u>NA</u>		15a. DECLASSIFICATION/DOWNGRADING SCHEDULE <u>NA</u>
17. SUPPLEMENTARY NOTES <u>The findings in this report are not to be construed as an official Department of the Army position, unless so designated by other authorized documents.</u>		
18. KEY WORDS (Continue on reverse side if necessary and identify by block number) <u>Image Modeling; Area Correlation; Radar Image Processing</u>		
19. ABSTRACT (Continue on reverse side if necessary and identify by block number) <u>The problem of modeling and processing radar images for tracking applications has been considered. Digital simulation experiments have been carried out for area correlation of a reference target image with on-board radar acquired images. Effects of misregistrations of radar height (scaling) and orientation (rotation) and those of high pass filtering of images have been studied. Use of image models based on finite difference approximation of partial differential equations (PDEs) has also been studied.</u>		

[The main body of the page is a large rectangular area, currently blank, which is likely a placeholder for a document or image. It is enclosed in a thin black border.]

TABLE OF CONTENTS

	Page
List of Figures	iii
List of Tables	v
List of Appendixes	v
Abstract	vi
I. Summary	1
II. Forward Looking Radar Image Modeling and Simulation	
2.1 Introduction	4
2.2 Area Correlation	5
2.2.1 Effect of Scaling	6
2.2.2 Effect of Rotation	6
2.2.3 Enhancement of FLR Images	7
2.2.4 Performance Evaluation	7
2.3 Modeling of FLR Images	8
2.4 Experimental Simulation Results	10
2.5 Conclusions and Future Work	13
III. Stochastic Image Modeling and Applications	38
IV. Real-Time RF Simulation of Re-entry Vehicles	43
V. Bibliography and References	46
Appendix I	47
Appendix II	56

ACCESSION FOR		
NTIS	NTIS Section	<input checked="" type="checkbox"/>
DDC	DDC Section	<input type="checkbox"/>
GRANDPRAIRIE		<input type="checkbox"/>
JUSTIFICATION		
BY _____		
DISTRIBUTION/AVAILABILITY CODES		
Dist.	AVAIL.	SPECIAL
A		

LIST OF FIGURES

	Page
1. FLR Geometry	9
2. Square ERTS Image used as SLR image	11
3. SLR image of Figure 2 with axes scaled by a factor 0.98	11
4. Ring-shaped (Radial) SLR image obtained from image of Fig. 2 with intensity in the area outside the ring set equal to the mean intensity of the image inside the ring	15
5. FLR-1 Image (see Table I for parameters)	16
6. FLR-1 Image of Figure 5 rotated clockwise by 2° .	16
7. Logarithm of the magnitude of the Fourier transform of the SLR image of Figure 2	17
8. Logarithm of the magnitude of the Fourier transform of the FLR image of Figure 5	17
9. α -Filtered image of the FLR image of Figure 5, $\alpha = 0.8$	18
10. α -Filtered image of the FLR image of Figure 5, $\alpha = 0.6$	18
11. Three Dimensional plot of the correlation function of square SLR and ring-shaped SLR image (shown in Fig. 2 and Fig.4)	19
12. Horizontal and vertical cross-sectional plots of the correlation function shown in Fig.11	20
13. Three dimensional plot of the cross correlation function of the SLR and FLR-2 images	21
14. Three dimensional plot of the cross correlation function of the Filtered SLR ($\alpha = .5$) and FLR-2 images	22
15. Three dimensional plot of the cross correlation function of the scaled (2%) and filtered ($\alpha = .5$) SLR image and rotated (2°) FLR-1 image	23
16. Three dimensional plot of the cross-correlation of the filtered ($\alpha = .5$) SLR and filtered ($\alpha = .5$) FLR-1 images	24
17. Horizontal and vertical cross-sections of the 3-D plot of Fig.13 across the peak.	25
18. Horizontal and vertical cross-sections of the 3-D plot of Fig.14 across the peak	26
19. Horizontal and vertical cross-sections of the cross-correlation function of rotated (2°) FLR-1 and filtered ($\alpha = .5$) SLR images across the peak	27

	Page
20. Horizontal and vertical cross-sections of the cross-correlation function of FLR-1 and scaled (2%) and filtered ($\alpha = .5$) SLR images across the peak	28
21. Horizontal and vertical cross-sections of the cross-correlation function of FLR-2 and scaled (2%) and filtered ($\alpha = .5$) SLR images across the peak	29
22. Horizontal and vertical cross-sections of the 3-D plot of Fig. 15 across the peak	30
23. Horizontal and vertical cross-sections of the 3-D plot of Fig. 16 across the peak	31
24. Signal to noise ratio of the correlation peak vs. the blur factor	32
25. Effect of scaling on the signal to noise ratio of the correlation peak	33
26. Effect of rotation on the signal to noise ratio of the correlation peak	34
27. Effect of Fourier domain α -filtering of the FLR-1 image on the signal to noise ratio of the correlation peak	35
28. Overview of real time hardware in the loop simulation of an area correlation guidance system	44
29. Detail architecture of real time RV simulation at U.S. MIRADCOM	45

LIST OF TABLES

I	Forward Looking Radar Parameters	36
II	Area Correlation Results	37

LIST OF APPENDIXES

I	Application of Partial Differential Equations in Image Restoration	47
II	Abstracts of Publications	56

ABSTRACT

The problem of modeling and processing radar images for tracking applications has been considered. Digital simulation experiments have been carried out for area correlation of a reference target image with on-board radar acquired images. Effects of misregistrations of radar height (scaling) and orientation (rotation) and those of high pass filtering of images have been studied. Use of image models based on finite difference approximation of partial differential equations (PDEs) has also been studied.

KEY WORDS: Image Modeling; Area Correlation; Radar Image Processing

I. SUMMARY

During the duration of this project the following progress has been made.

1. The problems associated with the overall goal of Forward Looking Radar Image Modeling and their real time simulation have been identified.

The basic problems are:

- a) Modeling and Identification of the Point Spread Function (PSF) of the FLR seeker.
- b) Stochastic Modeling of Image Fields and their use in image restoration and system identification
- c) Hardware encoding of FLR image model for real time RF simulation

2. A mathematical formulation of a typical FLR image has been developed. The FLR image can be synthesized digitally using this model and a reference Side Looking Radar (SLR) image. The model can also be identified if the statistical properties of SLR image are known. The underlying identification scheme would require a statistical model for two dimensional image fields. The FLR images are used for re-entry vehicle guidance via area correlation techniques. For a high signal to noise ratio of correlation peaks the FLR image (which is generally quite blurred) should be restored (or enhanced). Image restoration algorithms have been studied in this period using some new image models and some new algorithms have been shown to be associated with these models. (see attached list of publications). Further work is required to consider restoration schemes which include space varying nature of the point spread function (PSF) of the FLR imaging system.

3. The problem of stochastic image modeling has been studied in the framework of stochastic partial differential equations. Our results show that these models are quite effective and are often better than conventional image covariance models. These models have been applied for restoration of noisy images. Further work is required for application of these models to restoration of FLR images and for further refinement models.
4. Collaborative efforts were made with the Radio Frequency Simulation System (RFSS) laboratory of the Advanced Simulation Center (ASC) of the U.S. Missile Research and Development Command (MIRADCOM) for hardware in the loop simulation of the FLR image data. These efforts have produced a design of methodology of RFSS configuration to generate RF signals which represent FLR image data. Hardware design for transmission and reception of these signals still needs to be accomplished.

Personnel Supported During this Period

1. A.K. Jain - Project Director
2. J.R. Jain - Graduate Student
3. S.H. Wang - Graduate Student
4. R. Maedl - Technical and Secretarial Support

Papers published or in the process of being published under this grant.

1. A.K. Jain, "An Operator Factorization Method for Restoration of Blurred Images," IEEE Trans. on Comp. vol. C-26, pp. 1061-1071, Nov. 1977.
2. A.K. Jain and J.R. Jain, "Partial Differential Equations and Finite Differences in Image Processing, Part II: Image Restoration", to appear in IEEE Trans. on Auto. Control.
3. E. Angel and A.K. Jain, "Frame to Frame Restoration of Diffusion Images," to appear in IEEE Trans. on Auto. Control.
4. A.K. Jain, "Fast Inversion of Banded Toeplitz Matrices by Circular Decompositions," (submitted for publication).

A copy of the abstracts from these papers is attached with this report. Copies of reprints of published papers are being submitted separately to ARO.

II. FORWARD LOOKING RADAR IMAGE MODELING AND SIMULATION

2.1 Introduction

It is well known that for missile and aircraft guidance the area correlation between a target reference image, already stored in the vehicle, and a target image acquired by an on-board sensor could be utilized. The cross-correlation function of the two images is first obtained and the peak value of this function, indicating a match between the two images is located. The peak location is used to guide the vehicle in the direction of the target. It is assumed that a significant area of the target image is within the range of the on-board reference image; otherwise, no peak (or a false peak) could be located. Typically, this technique is used in the terminal phase of the flight.

For many terminal guidance applications the reference image is often generated by a side looking radar (SLR) or a high resolution sensor, while the on-board sensor is a forward looking radar (FLR) with significantly reduced resolution. Application of area correlation for guidance, therefore, requires an understanding of interactions between the actual scene and the radar sensing process. Also important for obtaining a good correlation peak is the proper registration of the two images. In practice two forms of misregistrations, namely, scaling and rotation of one image with respect to another are common. So it becomes important to know the effects of these misregistrations on the detection and the location of the peak. Here we report the results of the computer simulation experiments carried out to study the effects of FLR parameters, scaling, rotation and the filtering of FLR images on the area correlation.

In section 2.2 we describe the theoretical formulation of the experiments and the necessary assumptions. Modeling of FLR images from a given

SLR image is briefly described in Section 2.3. Experimental results of computer simulations are summarized in Section 2.4. Conclusions and suggested future work are given in Section 2.5.

2.2 Area Correlation

Let $u(x,y)$ and $v(x,y)$ denote the reference and the on-board generated images respectively. Then their area correlation function, denoted by $r(x,y)$, is given by

$$r(x,y) = \int_{-\infty}^{\infty} \int_{-\infty}^{\infty} u(x',y')v(x+x', y+y')dx'dy'. \quad (1)$$

In practice the images are available only over a finite area and hence the integration in (1) is performed only on the available area. For digital processing we approximate the integration in (1) by a summation given by

$$r(m,n) = \sum_{k=1}^N \sum_{l=1}^N u(k,l)v(k+m-1, l+n-1), \quad \frac{N}{2} - 1 \leq m,n \leq \frac{N}{2}, \quad (2)$$

where the available reference SLR signal has been digitized to $N \times N$ samples. Evaluation of $r(m,n)$ using (2) requires the knowledge of one of the images over a larger area than the other. If both images are available over the same area, as is assumed in our experiments, then replacing the function $v(i,j)$ by its two dimensional periodic repetition, allows one to compute (2) efficiently using discrete Fourier transform. If $U(m,n)$ and $V(m,n)$ denote the discrete Fourier transform (DFT) of sequences $u(k,l)$ and $v(k,l)$ respectively, then

$$R(m,n) = U^*(m,n)V(m,n), \quad 1 \leq m,n \leq N \quad (3)$$

gives the DFT of $r(k,l)$, where $*$ denotes the complex conjugate. The discrete correlation function $r(k,l)$ could then simply be computed by taking

the inverse DFT of $R(m,n)$. The use of fast Fourier transform (FFT) algorithm reduces the computation of (2) from N^4 to $O(N^2 \log_2 N)$. It should be noted that $r(k,l)$ computed as above is not centered around the origin. This could easily be done by shifting the samples in each coordinate axes by $\frac{N}{2}$ and reindexing.

2.2.1 Effect of Scaling

The effect of misregistration of radar heights, at which the reference and the on-board images are generated, is equivalent to scaling the axes of one of the images relative to the others. We assume the scaling of the reference image. A digital scaled image, with a scale factor of $s > 0$, could be approximated by

$$u_s(k,l) = u(\lfloor sk \rfloor, \lfloor sl \rfloor) \quad (4)$$

where $\lfloor a \rfloor$ denotes the highest integer less than or equal to a .

2.2.2 Effect of Rotation

Another common form of misregistration is the rotation of the live image with respect to the reference image along the vertical axis of FLR. As FLR images are radially scanned the rotation could be easily accomplished in polar coordinates. Let

$$v(r,\theta) = v(r \cos \theta, r \sin \theta)$$

then an FLR image rotated by an angle φ with respect to the reference image in clockwise direction is given by

$$v_\varphi(r,\theta) = v(r,\theta-\varphi)$$

and

$$v_{\varphi}(x,y) = v_{\varphi}(\sqrt{x^2+y^2}, \arctan(y/x)).$$

2.2.3 Enhancement of FLR Images

As noted earlier, the on-board generated FLR images have a poor resolution compared with the reference images. It is intuitively clear then, and also would be seen in the next section, that the resulting correlation function would not yield a desirable sharp peak and could even give a false peak. To remedy this it is desirable to enhance by some sort of high pass filtering of the FLR images before correlating them with reference images. There are various image enhancement techniques that are available in the literature. A class of techniques, known to be effective for blurred images performs filtering in the Fourier domain. This could be profitably exploited in our case as we are already taking the Fourier transform to get the correlation function. If $V(m,n)$ is the DFT of the discrete FLR image, then a typical Fourier domain filter, is

$$V_F(m,n) = F(V(m,n))$$

where F denotes a filter function, which could be linear or non-linear. An example of linear filter is the Wiener filter. A nonlinear high pass filter is, for example, the so-called α -filter given by

$$V_{\alpha}(m,n) = |V(m,n)|^{\alpha} e^{j2\pi \arg(V(m,n))} \quad 0 < \alpha \leq 1 \quad (5)$$

and (3) becomes

$$R_{\alpha}(m,n) = U^*(m,n) V_{\alpha}(m,n) .$$

2.2.4 Performance Evaluation

In practice $v(x,y)$ and $u(x,y)$ are not zero mean images. If the mean is

comparable to the variance of the image it adds a significant constant bias to the correlation function and the relative sharpness of the peak is decreased. So it is desirable to make one of the images zero mean, which in our case could be easily accomplished by setting the first element of the DFT of one of the images to zero. To study the effects of FLR parameters, misregistrations, and α -filter on the area correlation we define a criterion, called signal to noise ratio (or S/N), as

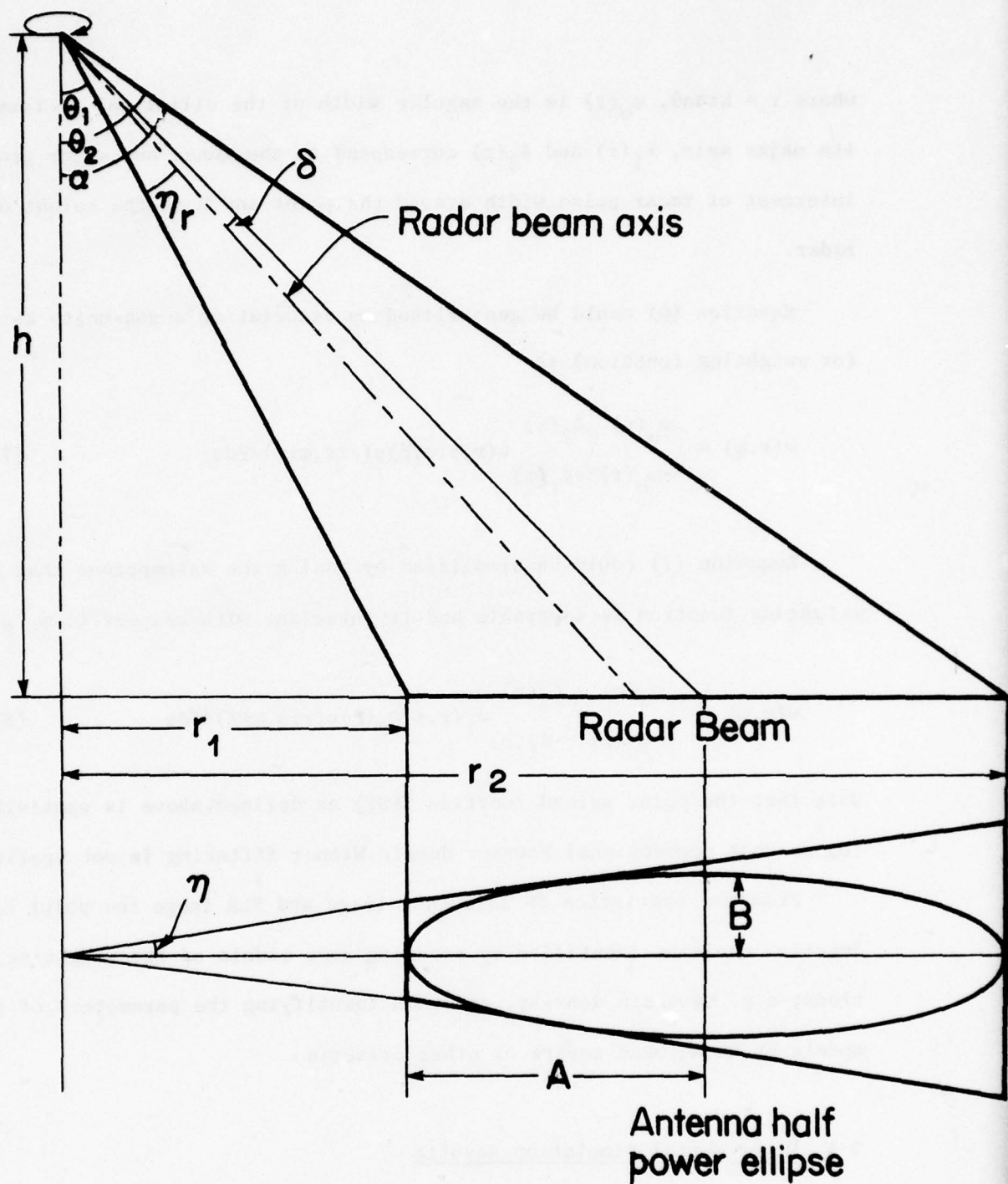
$$S/N = \frac{\text{Value of the Positive Peak}}{\text{Standard Deviation of the Correlation function}}$$

2.3 Modeling of FLR Images

For analyzing area correlation techniques it is necessary to have a model of the PSF of the FLR image. The model used in our experiments is based on the theory (which is also supported by practical data) that terrain reflectivity is independent of the viewing aspect angle except for extreme angles.

Figure 1 shows the FLR geometry. Scanning an offset antenna pattern around the vertical axis results in a ring or doughnut shaped coverage of ground. At any scan position, the resolution cells are bounded by the antenna half-power elliptical contour and a radial width equal to one-half of the vertical ground intercept of the radar pulse length. This width is a secant function of the range vector depression angle θ . The parameters of the half-power ellipse are also given in Figure 1. In polar coordinates the FLR signal could be expressed in terms of the reference scene, $u(r, \varphi)$ by

$$v(r, \varphi) = \int_{-\varphi_0(r)}^{\varphi_0(r)} \int_{-\ell_1(r)}^{\ell_2(r)} u(r+s, \varphi + \Psi) d\Psi ds \quad (6)$$



Cross Section of Radar Beam

$$A = (r_2 - r_1) / 2$$

$$B = h \cdot \tan(\eta) \sqrt{1 - (\tan(\delta) / \tan(\eta_r))^2} \cdot \cos(\delta) / \cos(\alpha)$$

Figure 1: FLR Geometry

where $r = h \tan \theta$, $\varphi_0(r)$ is the angular width of the elliptical contour from its major axis, $\ell_1(r)$ and $\ell_2(r)$ correspond to the inner and outer ground intercept of radar pulse width around the point and h is the height of the radar.

Equation (6) could be generalized by associating a non-unity kernel (or weighting function) as

$$v(r, \varphi) = \int_{-\varphi_0(r)}^{\varphi_0(r)} \int_{-\ell_1(r)}^{\ell_2(r)} w(r, s; \varphi, \Psi) u(r+s, \varphi+\Psi) d\Psi ds \quad (7)$$

Equation (7) could be simplified by making the assumptions that the weighting function is separable and is invariant with respect to φ , giving

$$v(r, \varphi) = \int_{-\varphi_0(r)}^{\varphi_0(r)} \int_{-\ell_1(r)}^{\ell_2(r)} w_1(r, s) w_2(\Psi) u(r+s, \varphi+\Psi) d\Psi ds \quad (8)$$

Note that the point spread function (PSF) as defined above is spatially varying so that conventional Fourier domain Wiener filtering is not applicable.

From the statistics of reference image and FLR image the point spread function could be identified by assuming some models of the weighting functions, e.g. Gaussian density, and then identifying the parameters of these models by using mean square or other criteria.

2.4 Experimental Simulation Results

Figure 2 shows a 256 x 256 remotely sensed six-bit image. Considering this as only a single quadrant of a reference image, a 90° segment of an FLR image was simulated using Eqn. (6). The blur-factor as reported in our experiment is roughly a measure of average number of samples of the reference image summed to get the intensity at each sample of FLR. Also, the FLR images have been normalized to have the same mean square energy as

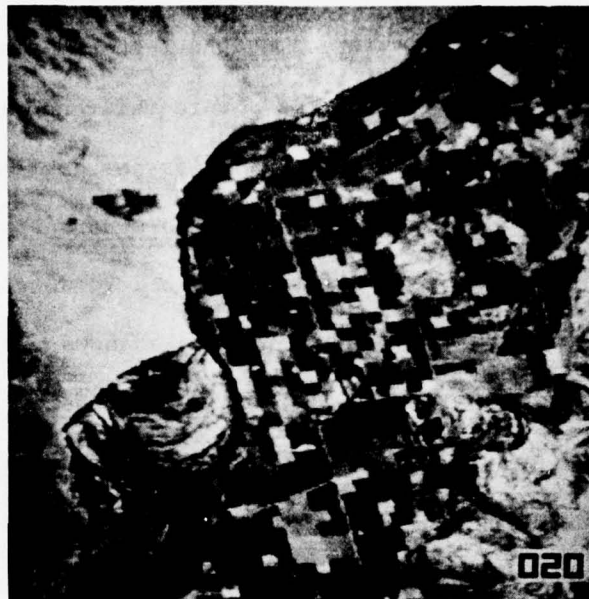


FIGURE 2

Square ERTS Image Used as SLR Image



FIGURE 3

SLR Image of Figure 2 With Axes Scaled by a Factor 0.98

the reference image within the area covered by the FLR image.

Figure 3 shows a scaled reference image corresponding to Figure 2 with a scale factor of 0.98. To simulate a doughnut-shaped quadrant of an FLR image a doughnut-shaped quadrant of the square reference image was created and sampled in polar coordinates with 4 samples per degree in azimuth and 200 samples along the elevation. Figure 4 shows this corresponding to Figure 2. From this three different FLR images as discussed in Section 2.3 with parameters shown in Table I were obtained. Figure 5 shows one such image. Both in Figure 4 and Figure 5 the image intensity outside the doughnut is replaced by its mean intensity. For calculating the correlation function the polar FLR images were transformed to cartesian coordinates square images. Figure 6 shows the FLR image of Figure 5 with a 2° misregistration. Figure 7 and Figure 8 show the logarithm of the magnitude of the discrete Fourier transform of the images of Figure 2 and Figure 5 respectively. Figure 9 and Figure 10 are the high pass filtered images corresponding to the FLR image of Figure 5.

The results of digital correlation experiments are summarized in Table II. Figure 11 and Figure 12 show the correlation function and its cross-section for images of Figure 2 and Figure 4. To improve correlation peaks the reference image was high pass filtered ($\alpha = .05$).

Figures 13-16 show the three dimensional plots of the correlation functions for some of the entries of Table II. Here every fourth sample of the 256×256 correlation function, has been plotted. Figures 17-23 show the horizontal and the vertical cross-sections of some of the correlation functions across the peak.

Figure 24 shows the effect of FLR beam pulse width product (or equivalently blur factor) on the signal to noise ratio for the original and filtered reference image. Figure 25 shows the effect of scaling the axes of the

reference image on the signal to noise ratio. Figure 26 shows the effects of rotating the FLR image and the combined effect of scaling and rotation on the signal to noise ratio. Finally, Figure 27 shows the effect of the filter parameter α on the signal to noise ratio.

These experiments show that high-pass filtering improves the correlation results considerably. From Figure 24 we see that the signal to noise ratio of the cross-correlation between the reference image and FLR images is much lower than that of the autocorrelation of reference image even for small amount of blur. This is mostly because of the space-variant nature of the FLR blurring mechanism rather than the low resolution of the FLR images.

Figure 25 shows that the signal to noise ratio drops sharply with the scaling of axes and is almost linear. In the presence of large rotational misregistration the scaling has only marginal effect, as could be seen from Figure 26.

2.5 Conclusions and Future Work

As demonstrated by results in the previous section the enhancement of the on-board generated FLR images using Fourier domain high pass filtering is quite useful in a more unambiguous location of the correlation peak. Although this simple and adhoc technique gives good results, it does not perform the optimum filtering of the point spread function of the FLR, which is space-variant along elevation. A better technique is to identify the models of the PSF and then do easily implementable optimum or sub-optimum filtering.

Stochastic modeling of the reference image and the FLR image is another area for future research. A considerable progress has been made recently in this area for certain class of images (see Appendixes I and II). These

models could be used for identification of PSF and also in applying the statistical detection theory to identify and locate the correlation peak.

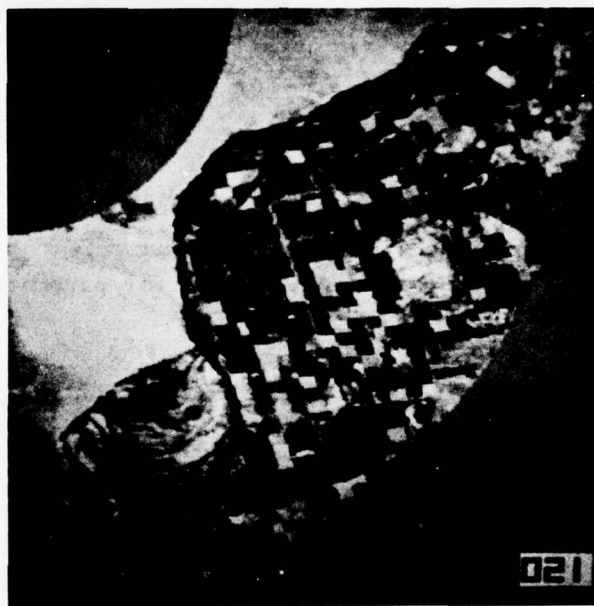


FIGURE 4

Ring-shaped (Radial) SLR Image obtained from Image of Fig. 2 with intensity in the area outside the ring set equal to the mean intensity of the image inside the ring



FIGURE 5
FLR-1 Image (see Table I for parameters)

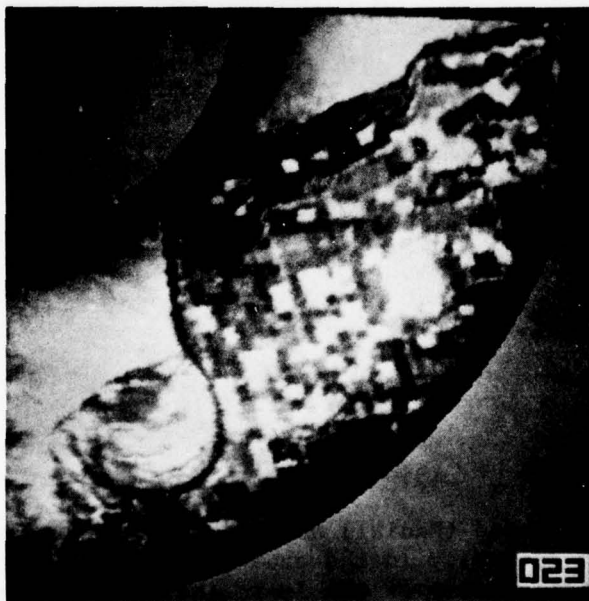


FIGURE 6
FLR-1 Image of Figure 5 Rotated Clockwise by 2°

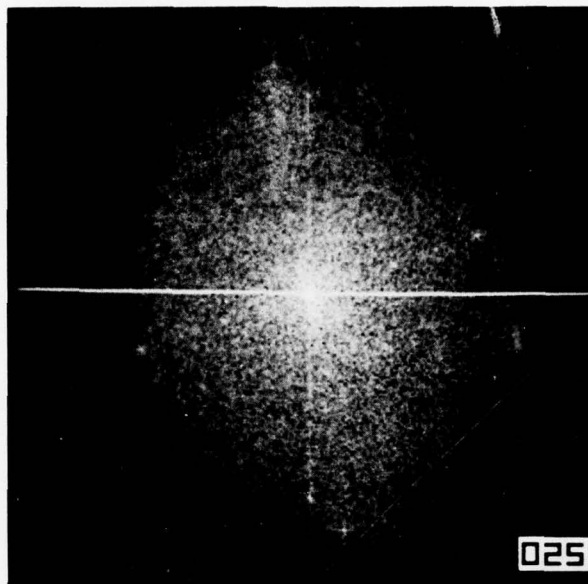


FIGURE 7
Logarithm of the magnitude of the Fourier transform of
SLR Image of Figure 2

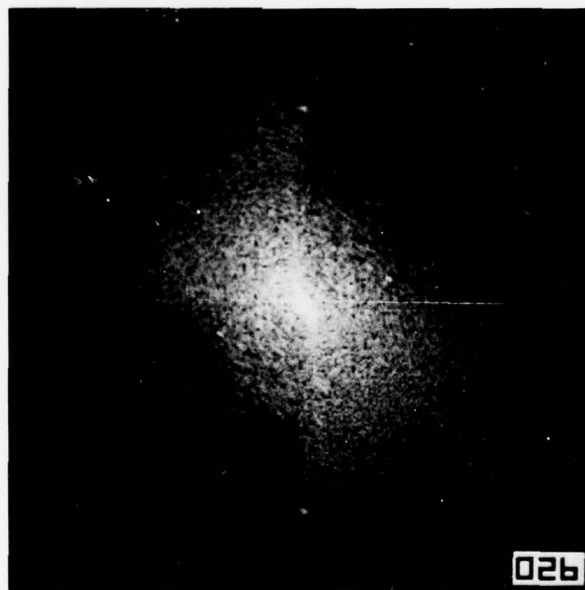


FIGURE 8
Logarithm of the magnitude of the Fourier transform of
FLR Image of Figure 5

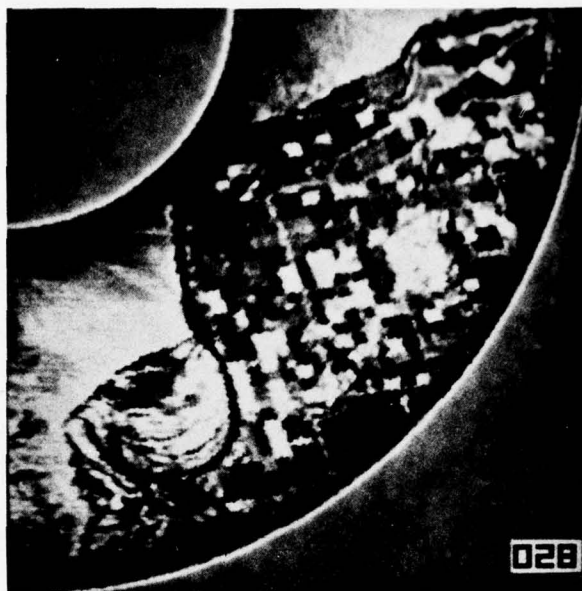


FIGURE 9
 α -Filtered image of the FLR Image of Figure 5, $\alpha = 0.8$



FIGURE 10
 α -Filtered image of the FLR image of Figure 5, $\alpha = 0.6$

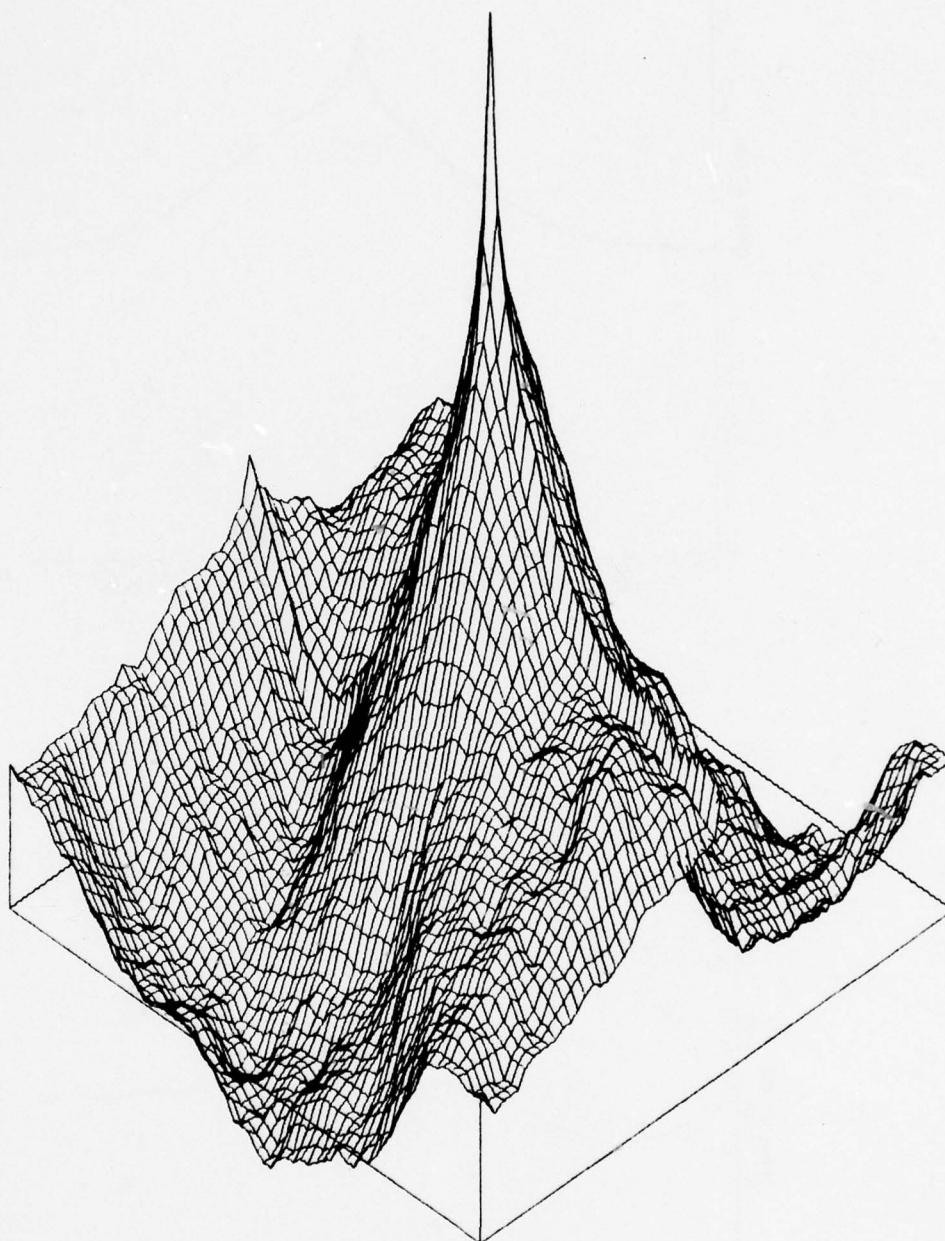


Figure 11: Three Dimensional Plot of the Correlation Function of Square SLR and Ring-shaped SLR image (shown in Fig. 2 & Fig. 4)

THIS PAGE IS BEST QUALITY PRACTICABLE
FROM COPY FURNISHED TO DDC

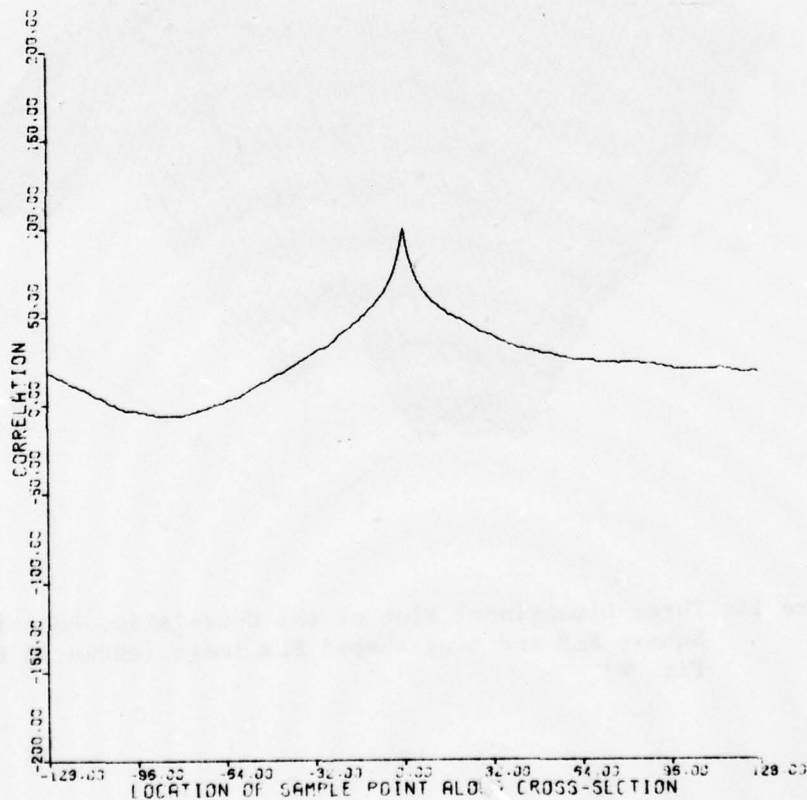
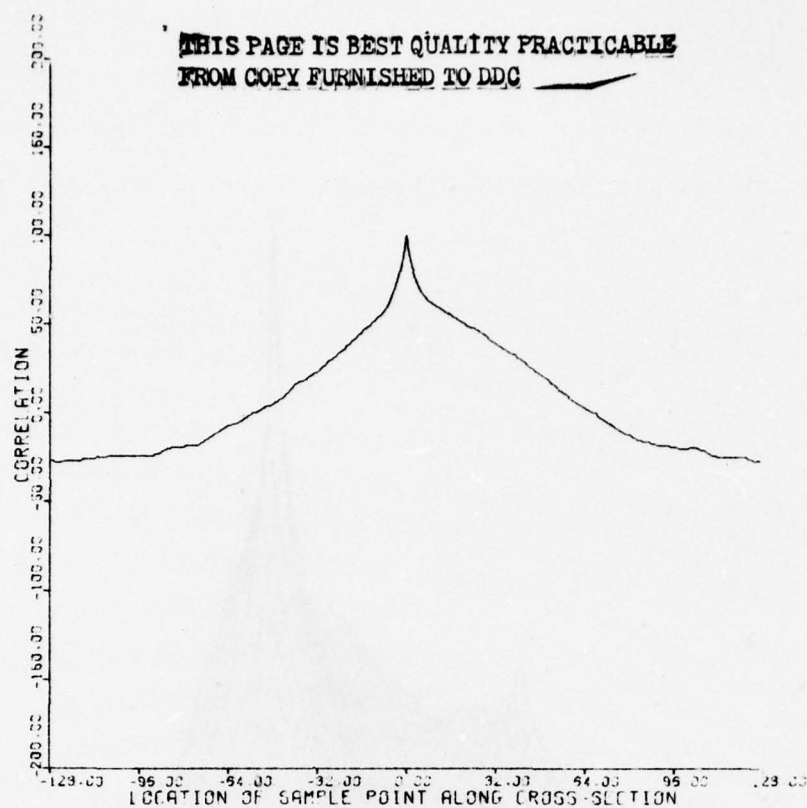


Figure 12: Horizontal and vertical cross-sectional plots of the correlation function shown in Fig. 11

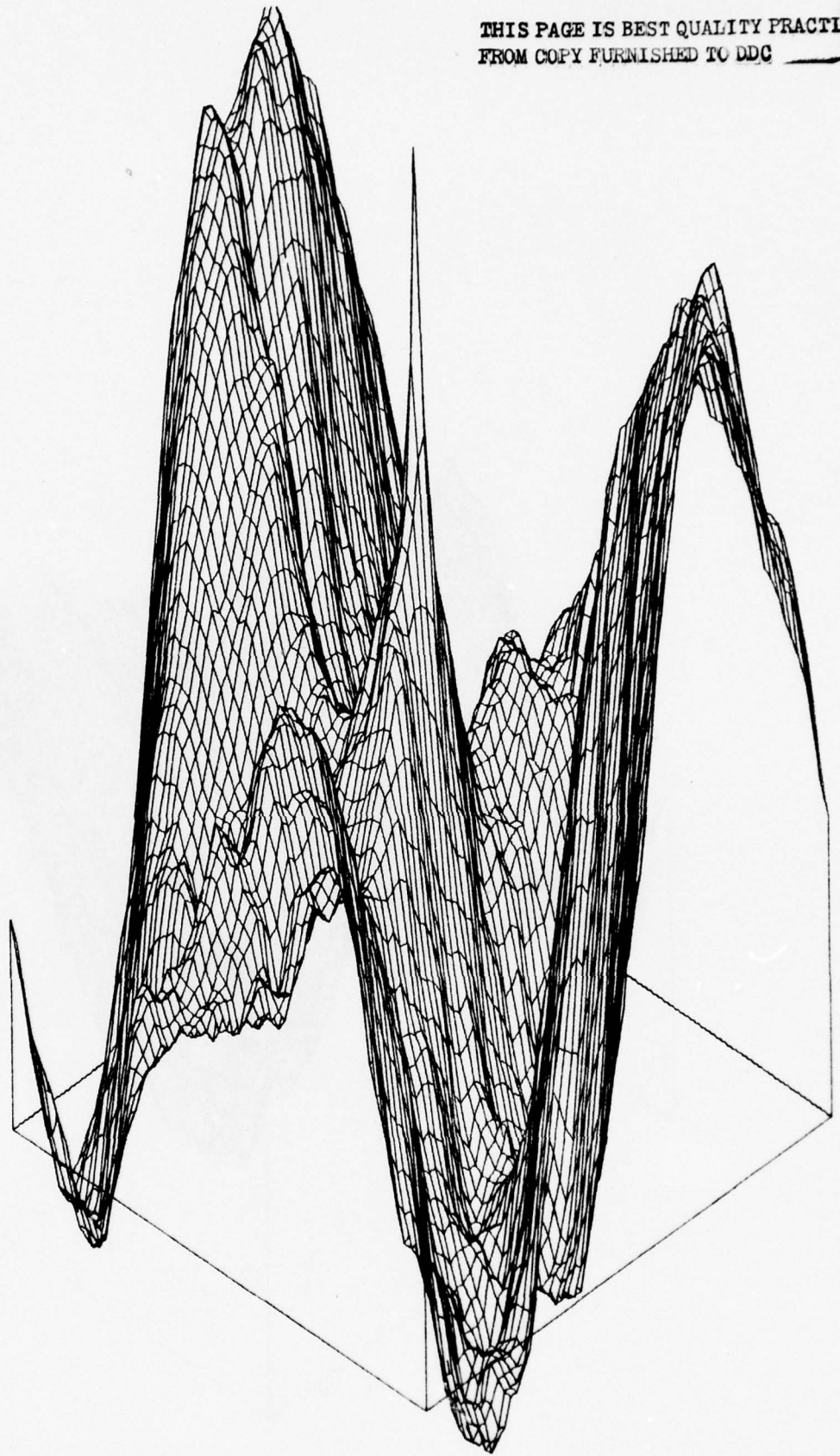


Figure 13: Three dimensional plot of the cross correlation function of the SLR and FLR-2 images

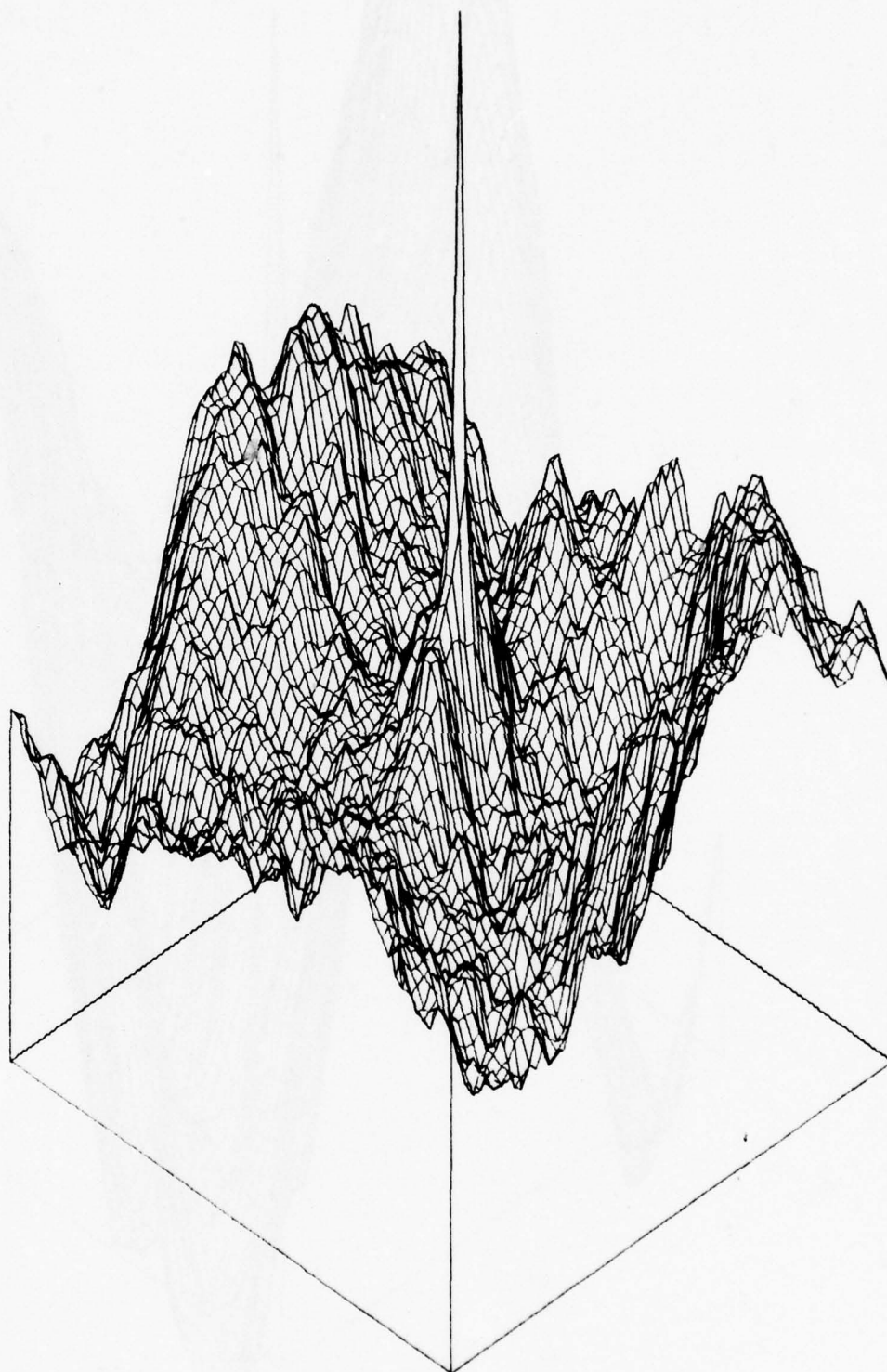


Figure 14: Three dimensional plot of the cross correlation function of the Filtered SLR ($\alpha = .5$) and FLR-2 images

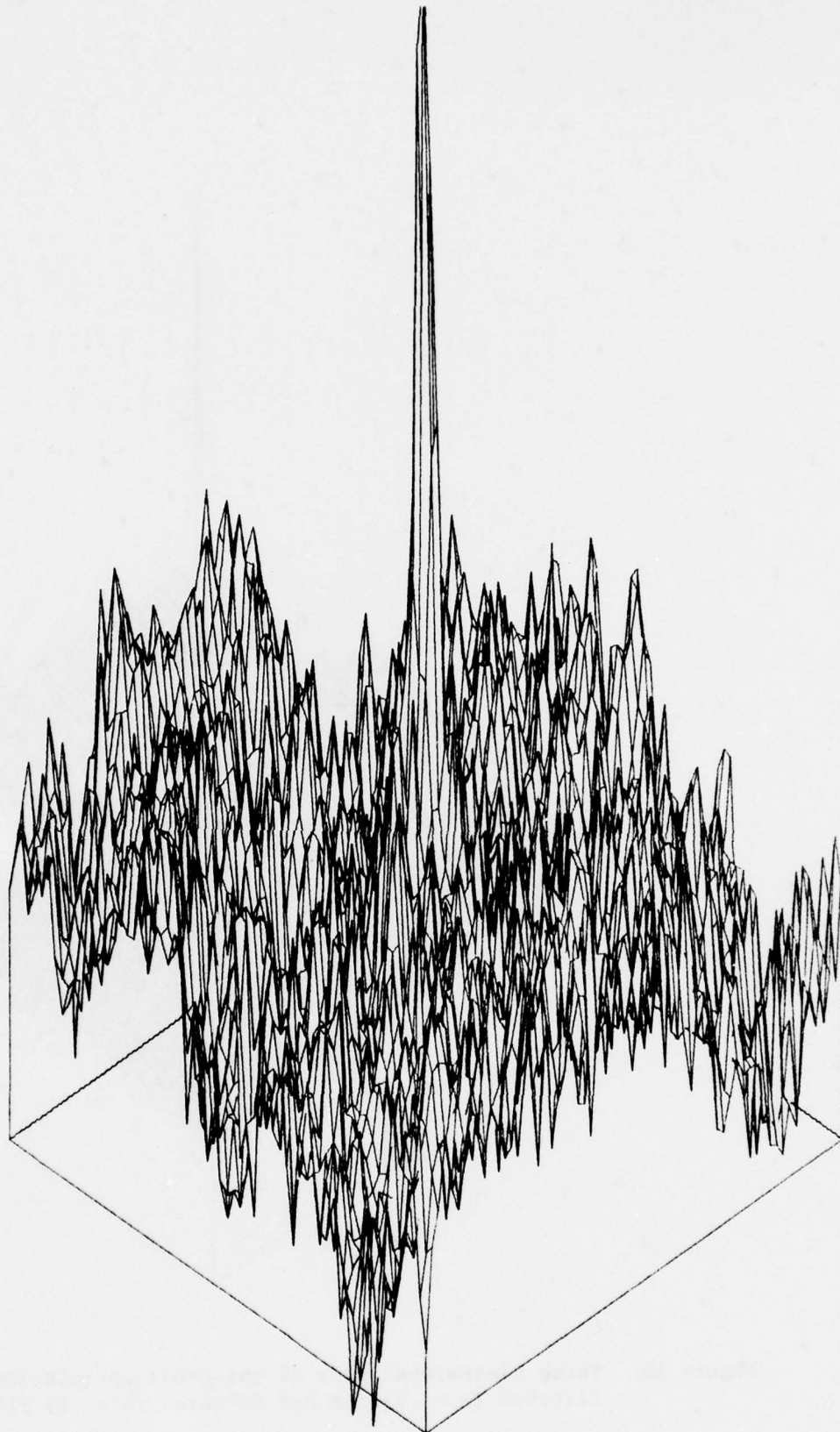


Figure 15: Three dimensional plot of the cross correlation function of the scaled (2%) and filtered ($\alpha = .5$) SLR image and rotated (2°) FLR-1 image

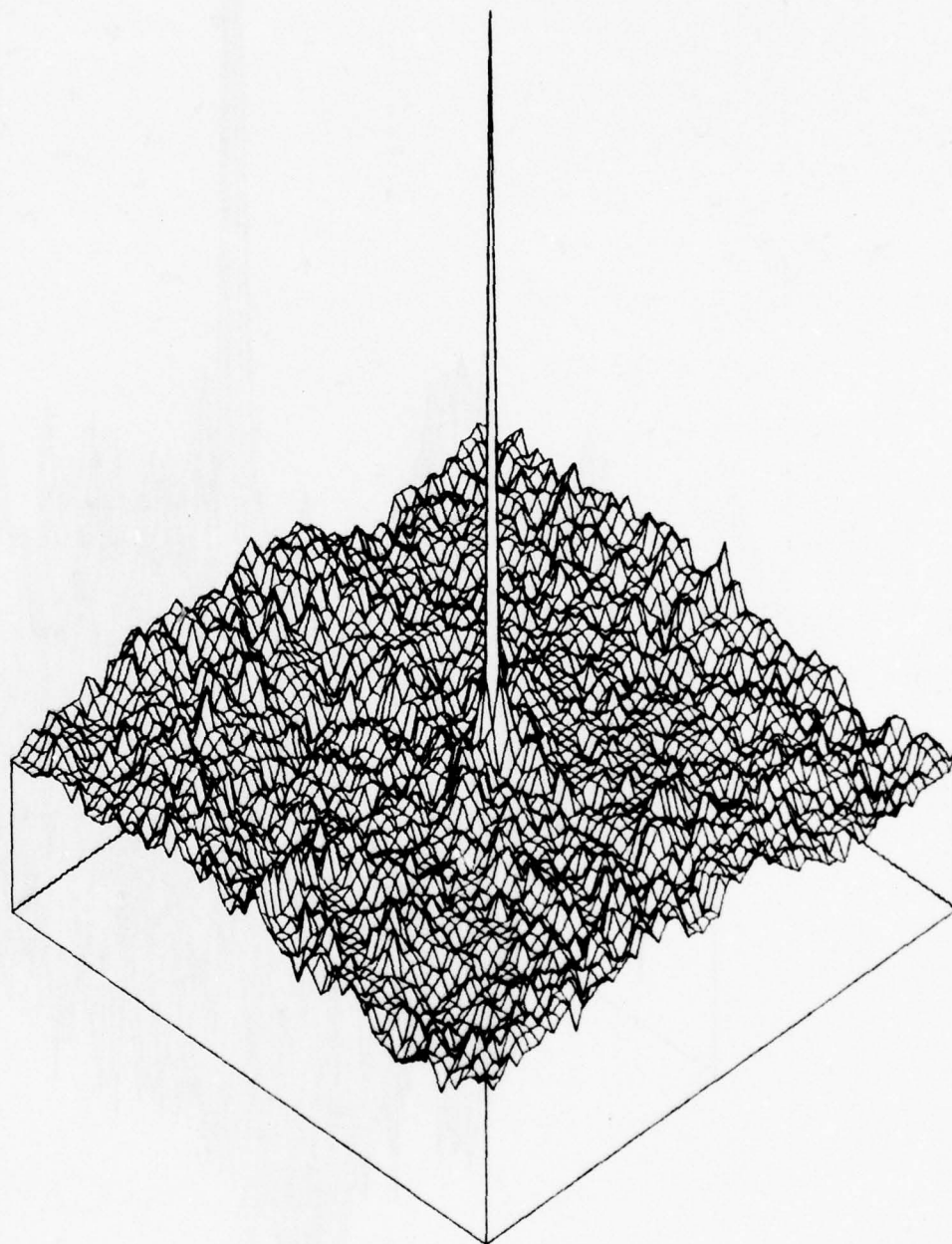


Figure 16: Three dimensional plot of the cross correlation of the filtered ($\alpha = .5$) SLR and filtered ($\alpha = .5$) FLR-1 image

THIS PAGE IS BEST QUALITY PRACTICABLE
FROM COPY FURNISHED TO DDG

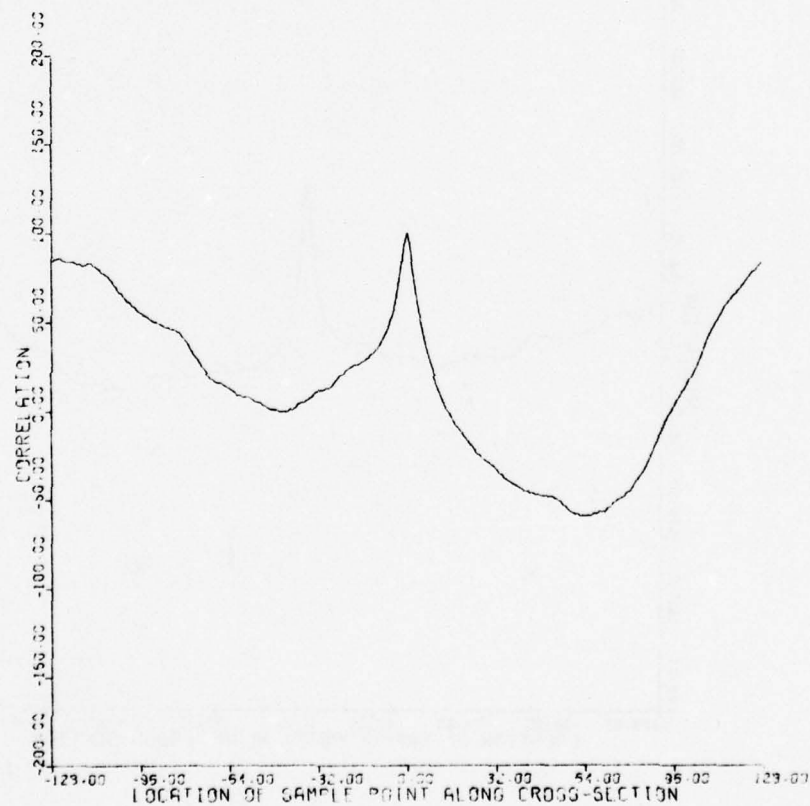
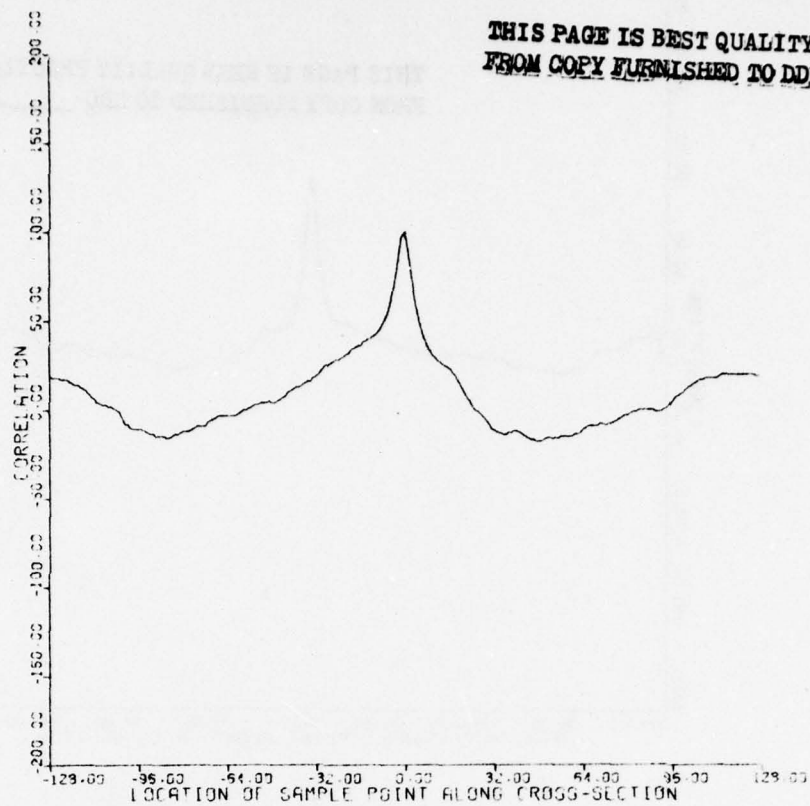


Figure 17: Horizontal and vertical cross-sections of the 3-D plot of Fig. 13 across the peak

THIS PAGE IS BEST QUALITY PRACTICABLE
FROM COPY FURNISHED TO DDG

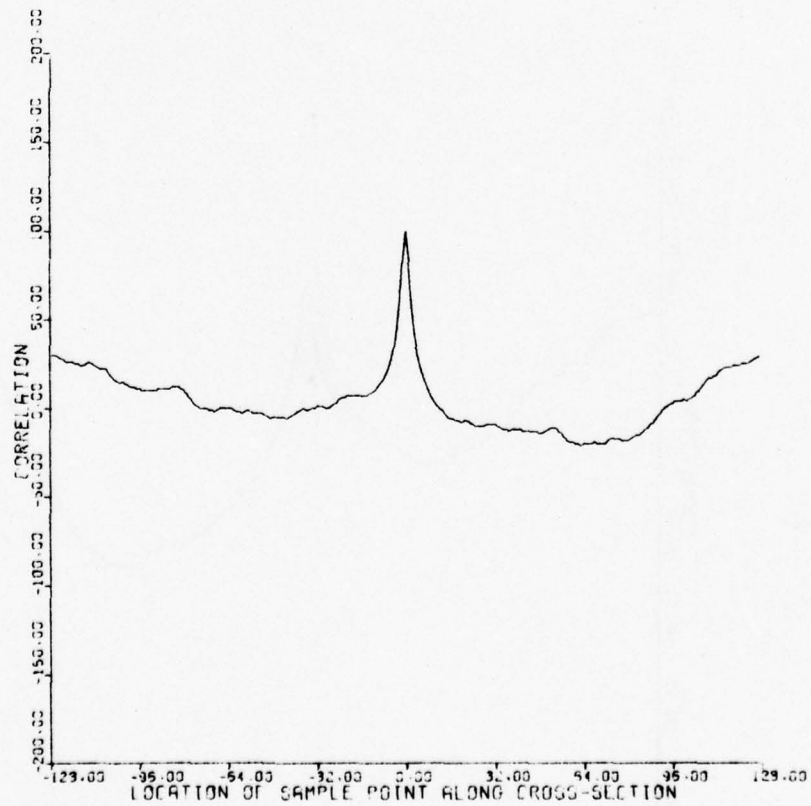
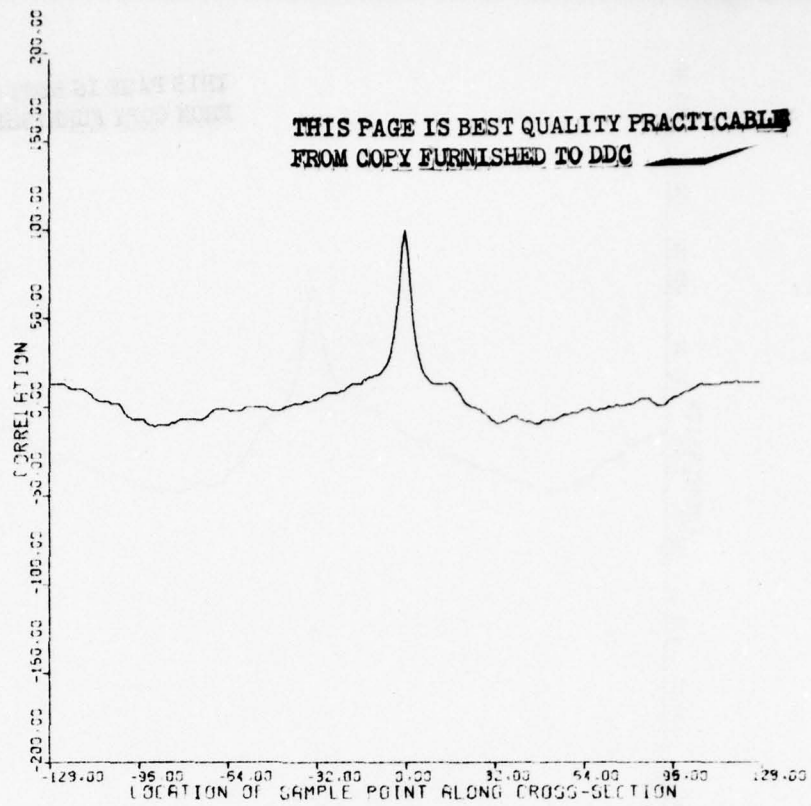


Figure 18: Horizontal and vertical cross-sections of the 3-D plot of Fig. 14 across the peak.

THIS PAGE IS BEST QUALITY PRACTICABLE
FROM COPY FURNISHED TO DDC

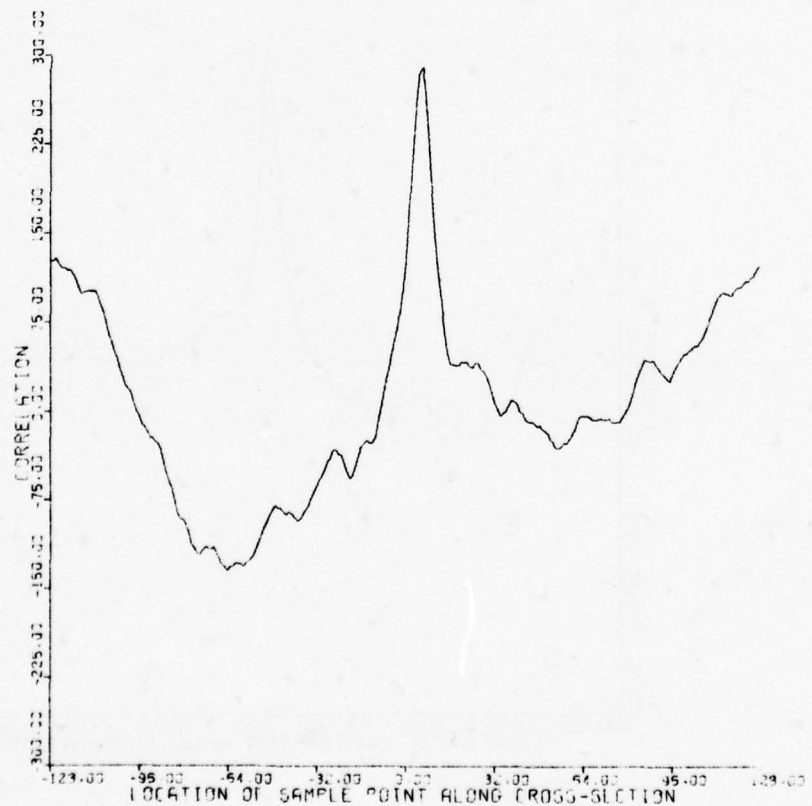
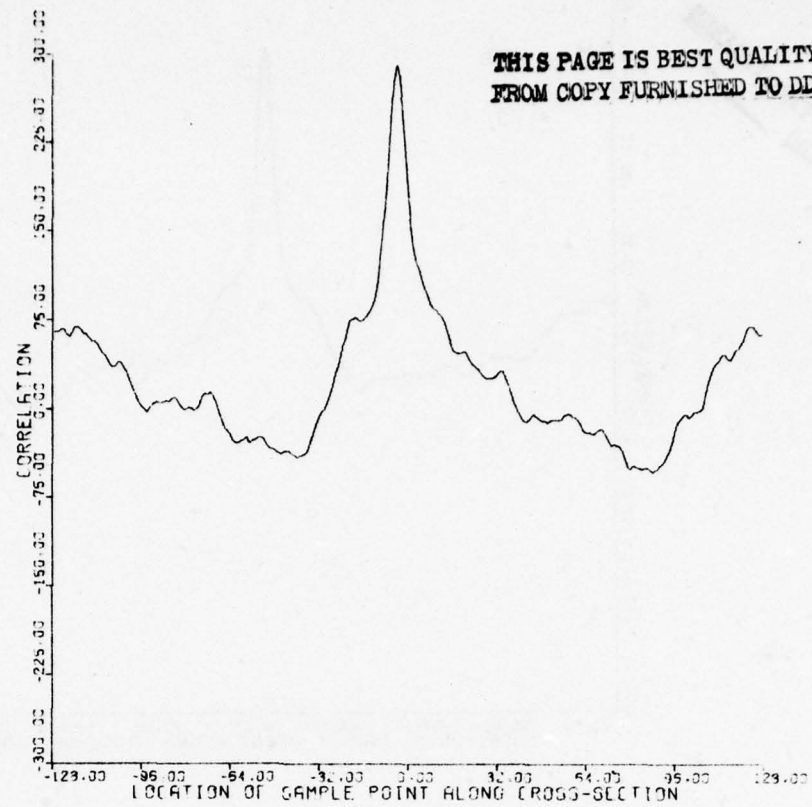


Figure 19: Horizontal and vertical cross-sections of the cross correlation function of rotated (2°) FLR-1 and filtered ($\alpha = .5$) SLR images across the peak

THIS PAGE IS BEST QUALITY PRACTICABLE
FROM COPY FURNISHED TO DDG

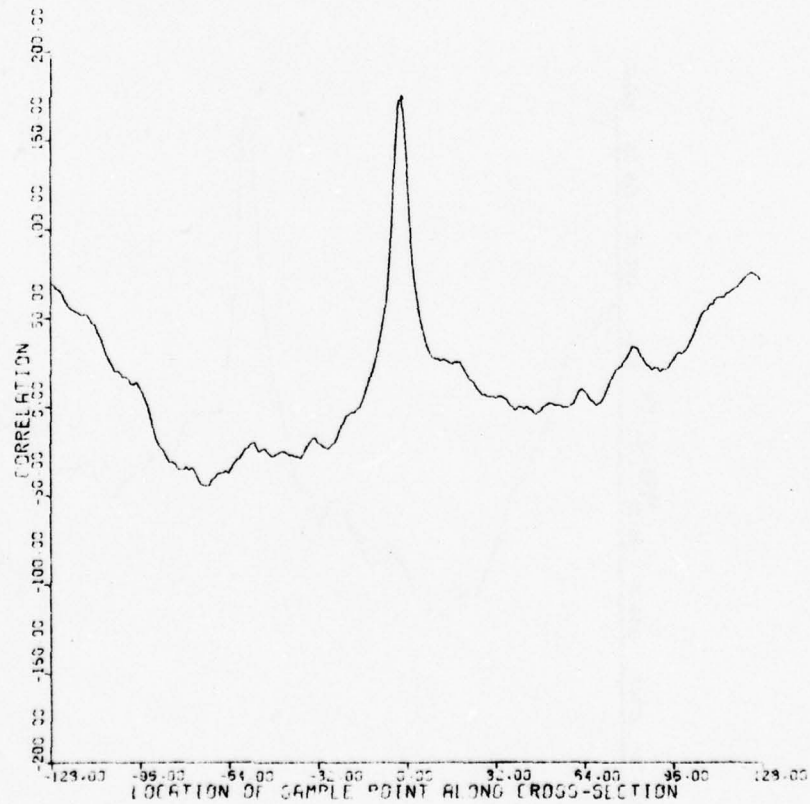
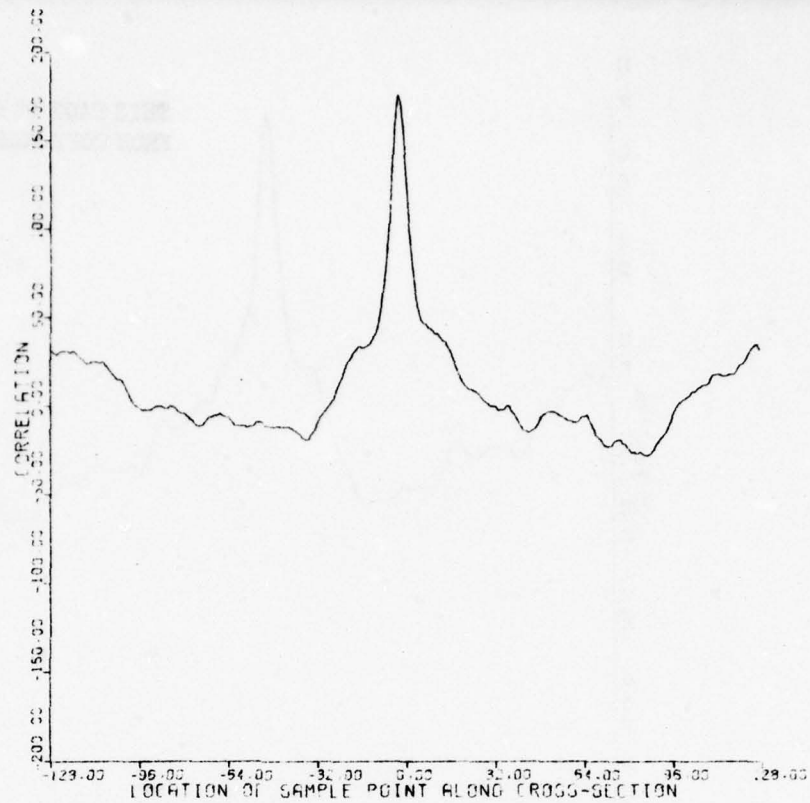


Figure 20: Horizontal and vertical cross-sections of the cross correlation function of FLR-1 and scaled (2%) and filtered ($\alpha = .5$) SLR images across the peak

THIS PAGE IS BEST QUALITY PRACTICABLE
FROM COPY FURNISHED TO DDC

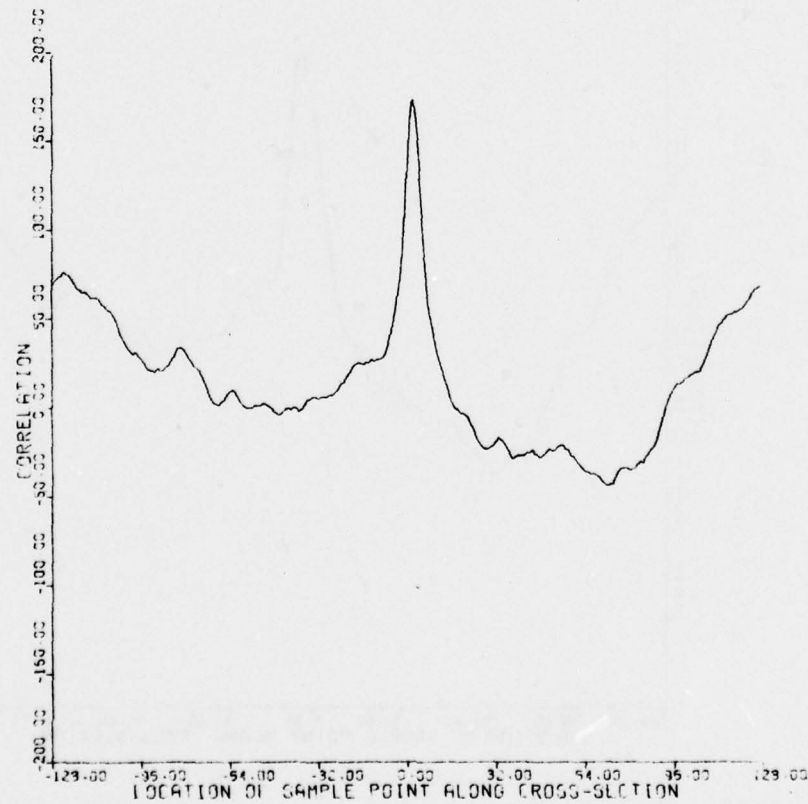
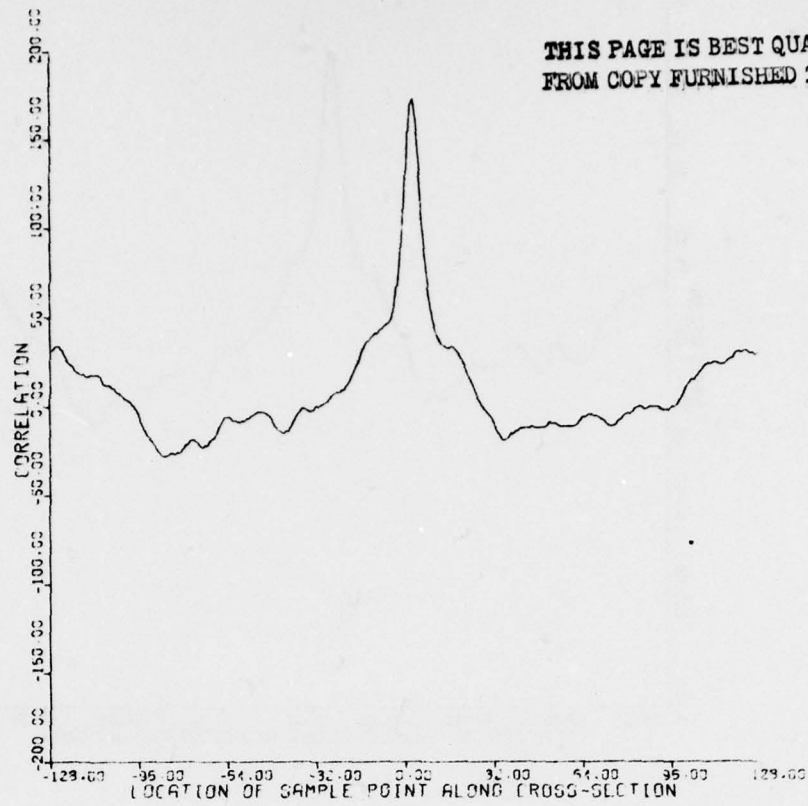


Figure 21: Horizontal and vertical cross-sections of the cross correlation function of FLR-2 and scaled (2%) and filtered ($\alpha = .5$) SLR images across the peak

THIS PAGE IS BEST QUALITY PRACTICALLY
FROM COPY FURNISHED TO DDG

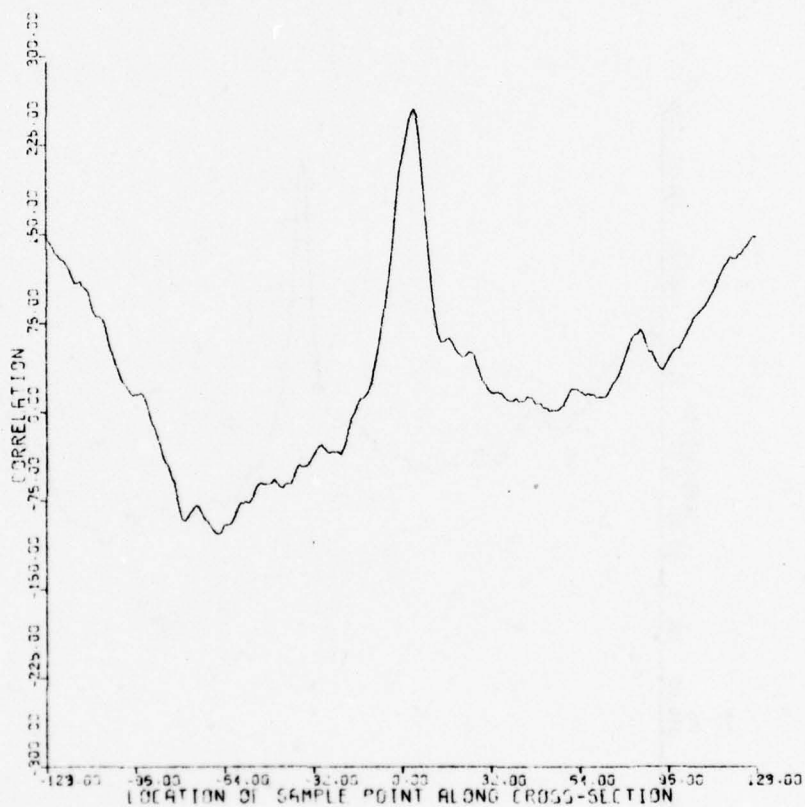
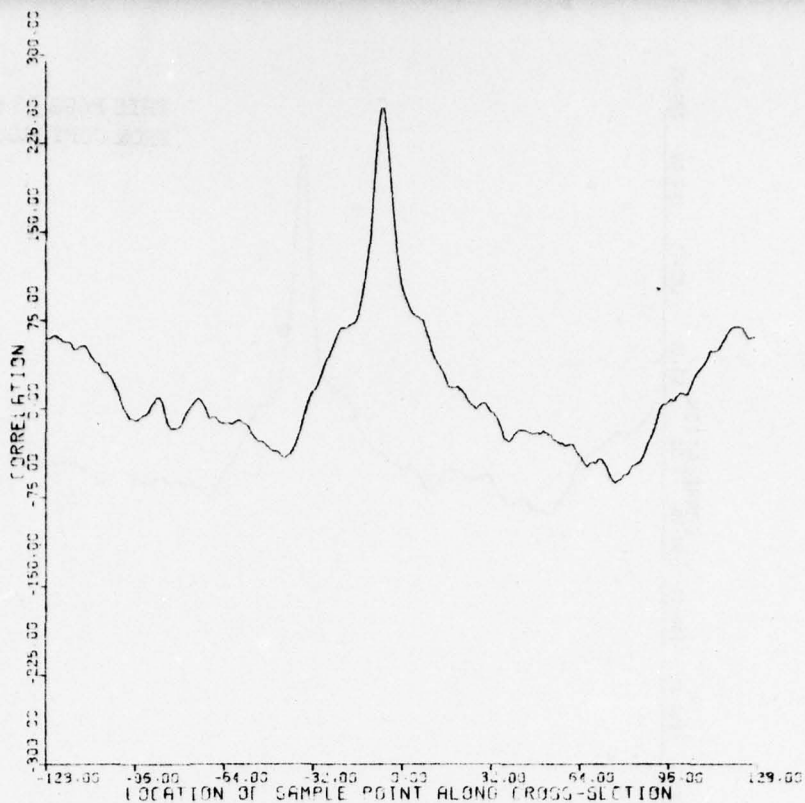


Figure 22: Horizontal and vertical cross-sections for the 3-D plot of Figure 15 across the peak

THIS PAGE IS BEST QUALITY PRACTICABLE
FROM COPY FURNISHED TO DDG

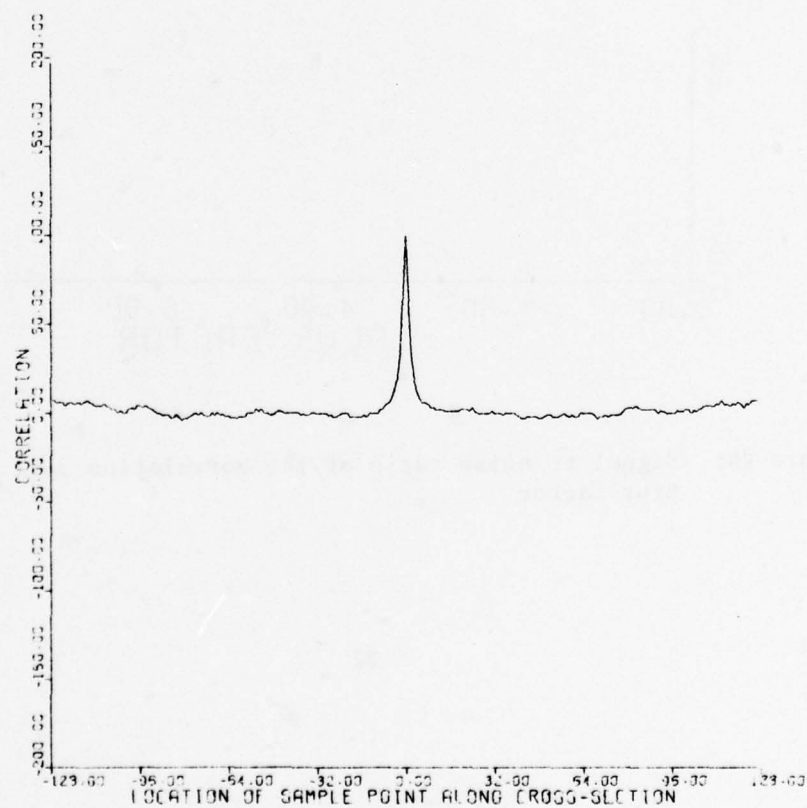
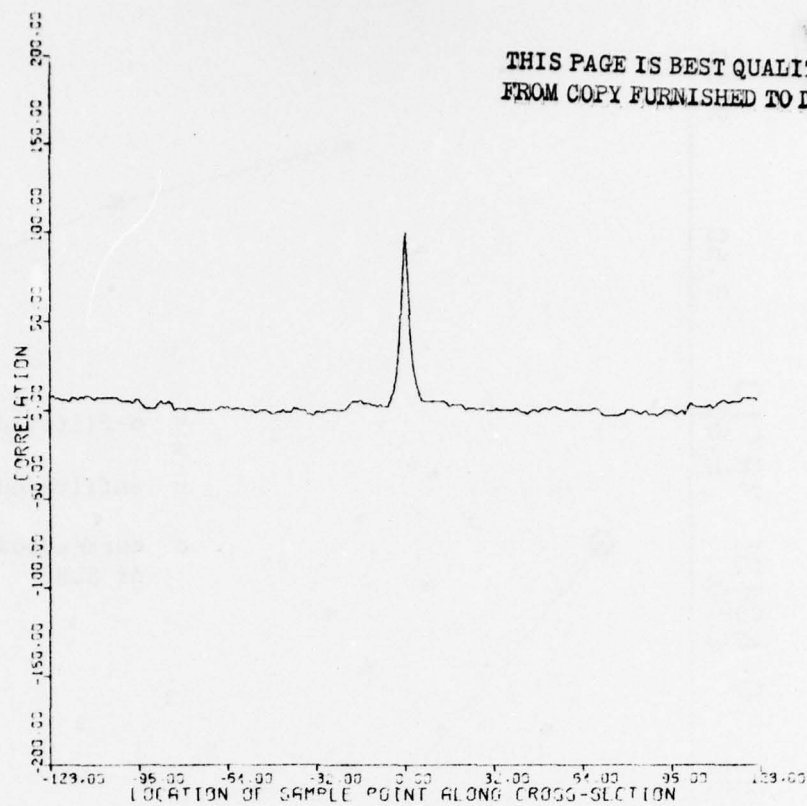


Figure 23: Horizontal and vertical cross-sections of the 3-D
Plot of Figure 16 across the peak

THIS PAGE IS BEST QUALITY PRACTICABLE
FROM COPY FURNISHED TO DDG

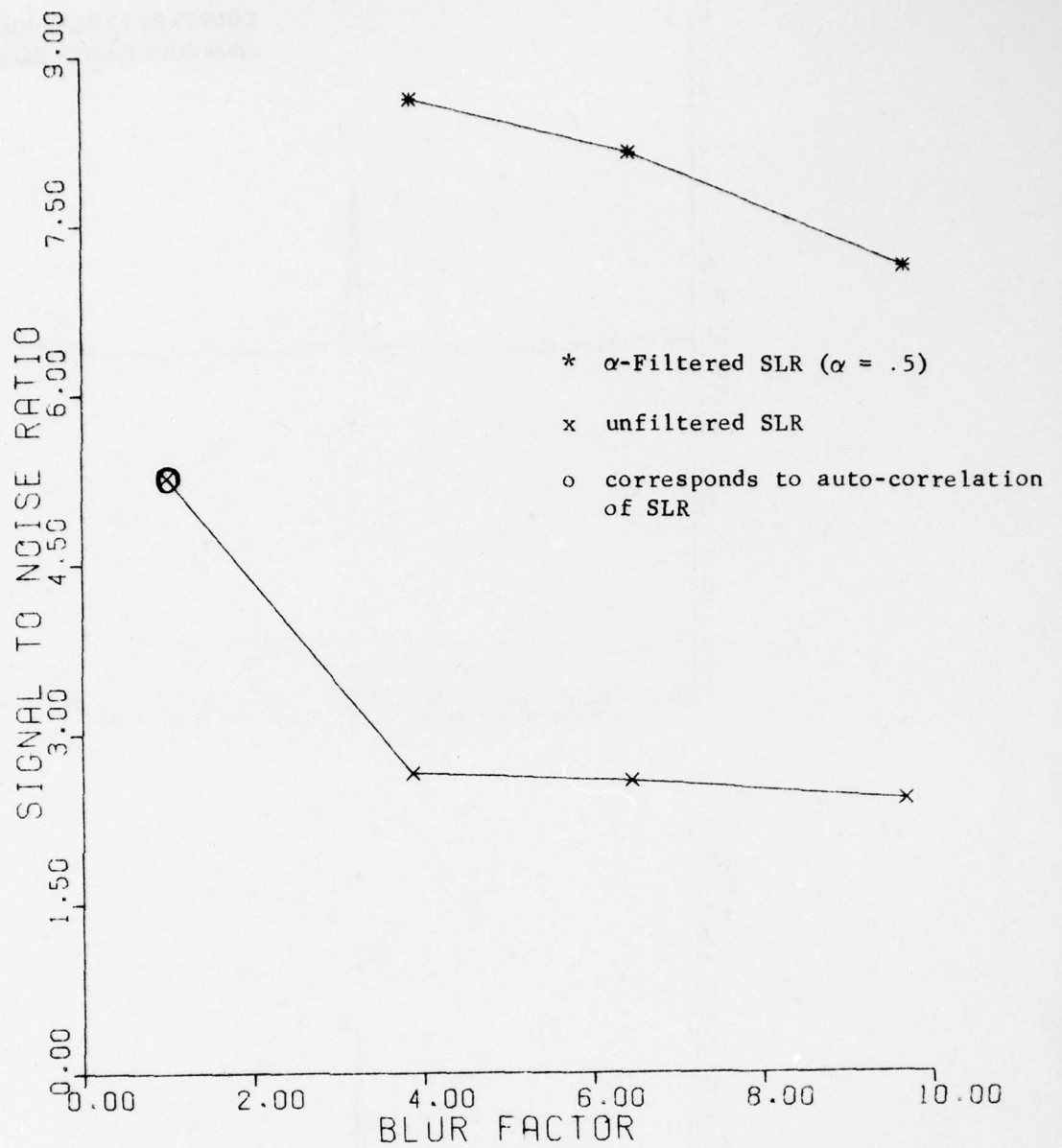


Figure 24: Signal to noise ratio of the correlation peak vs. the Blur factor

THIS PAGE IS BEST QUALITY PRACTICABLE
FROM COPY FURNISHED TO DDG

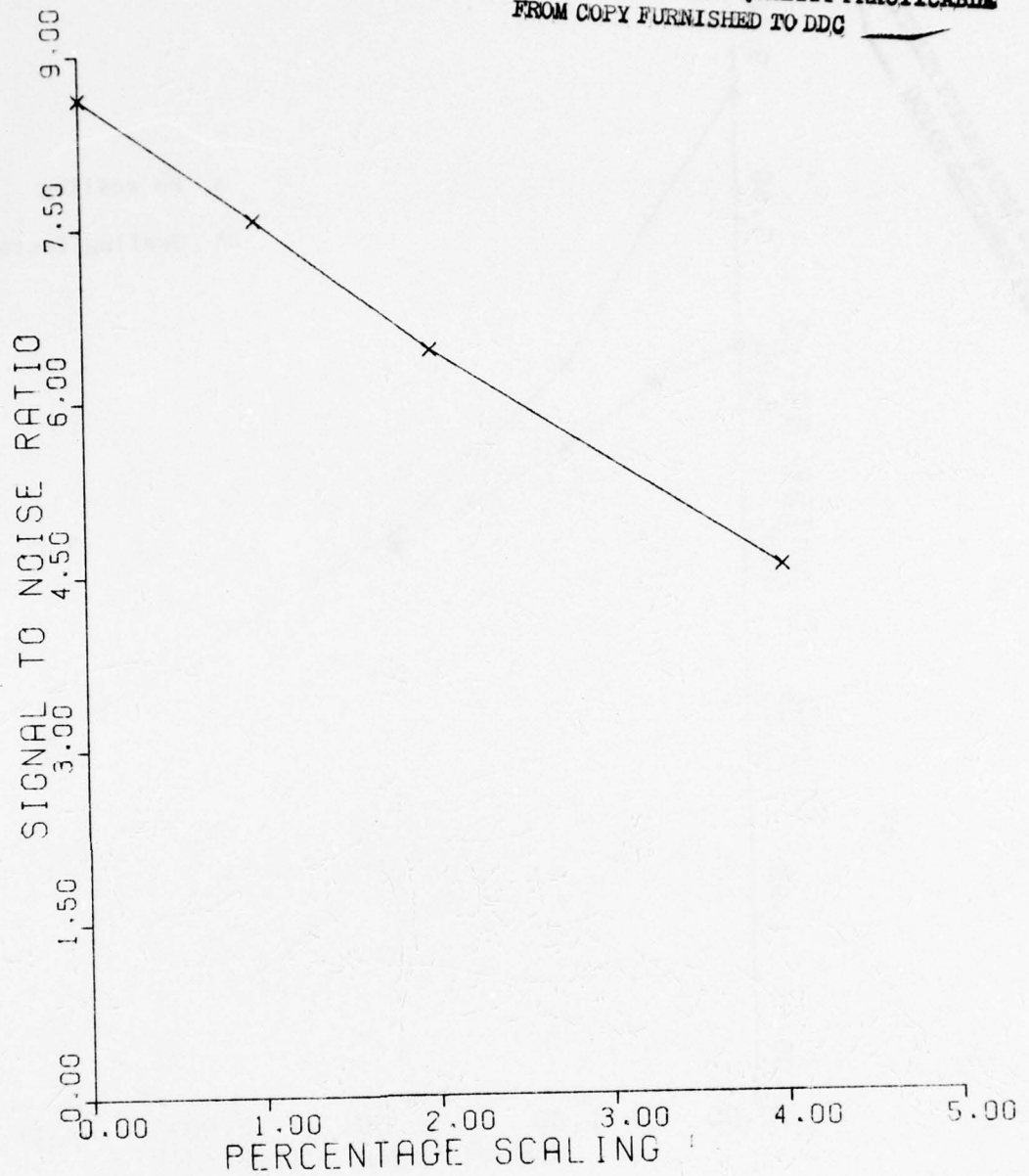


Figure 25: Effect of scaling on the signal to noise ratio of the correlation peak

THIS PAGE IS BEST QUALITY PRACTICABLE
FROM COPY FURNISHED TO DDC

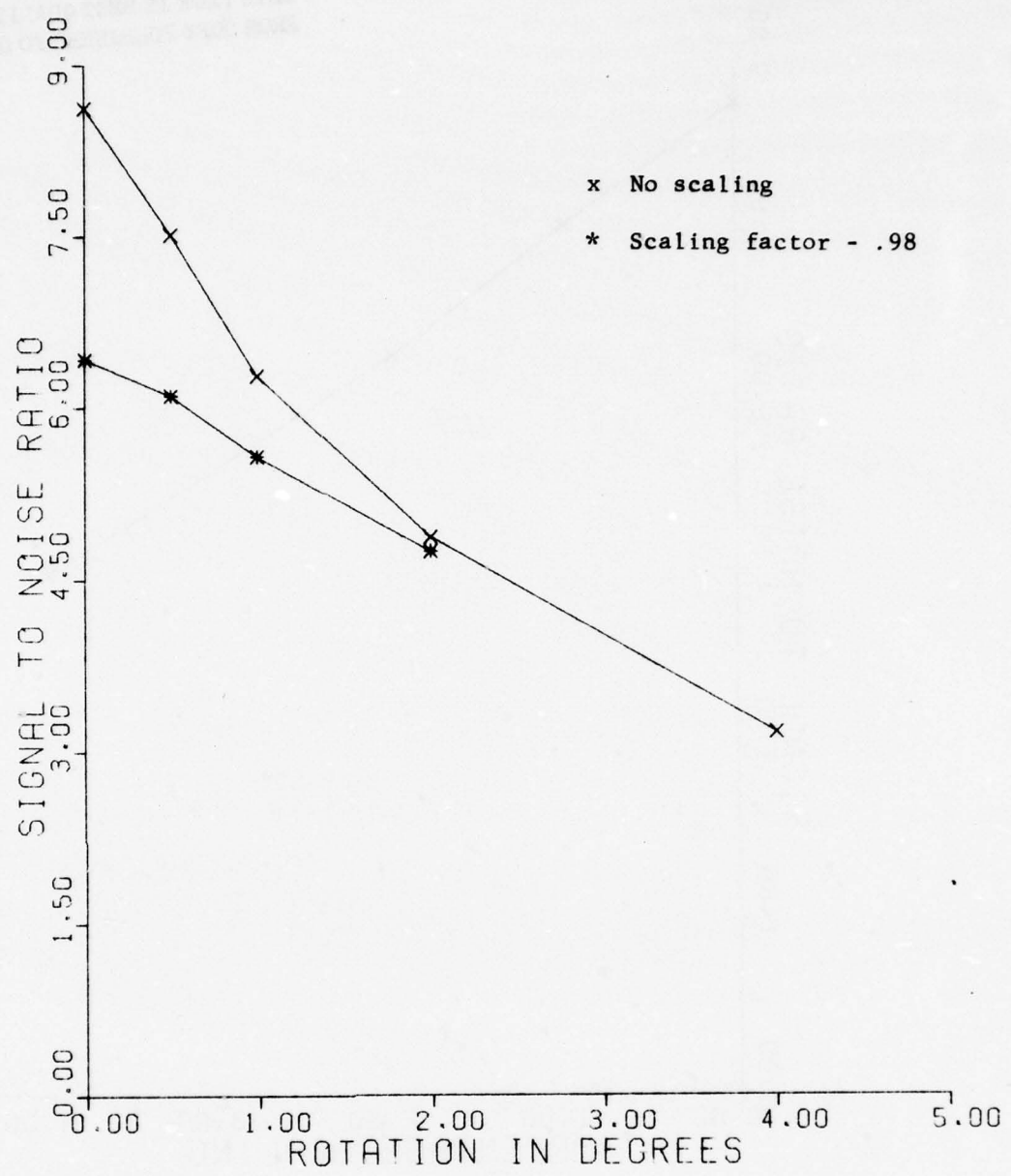


Figure 26: Effect of rotation on the signal to noise ratio of the correlation peak

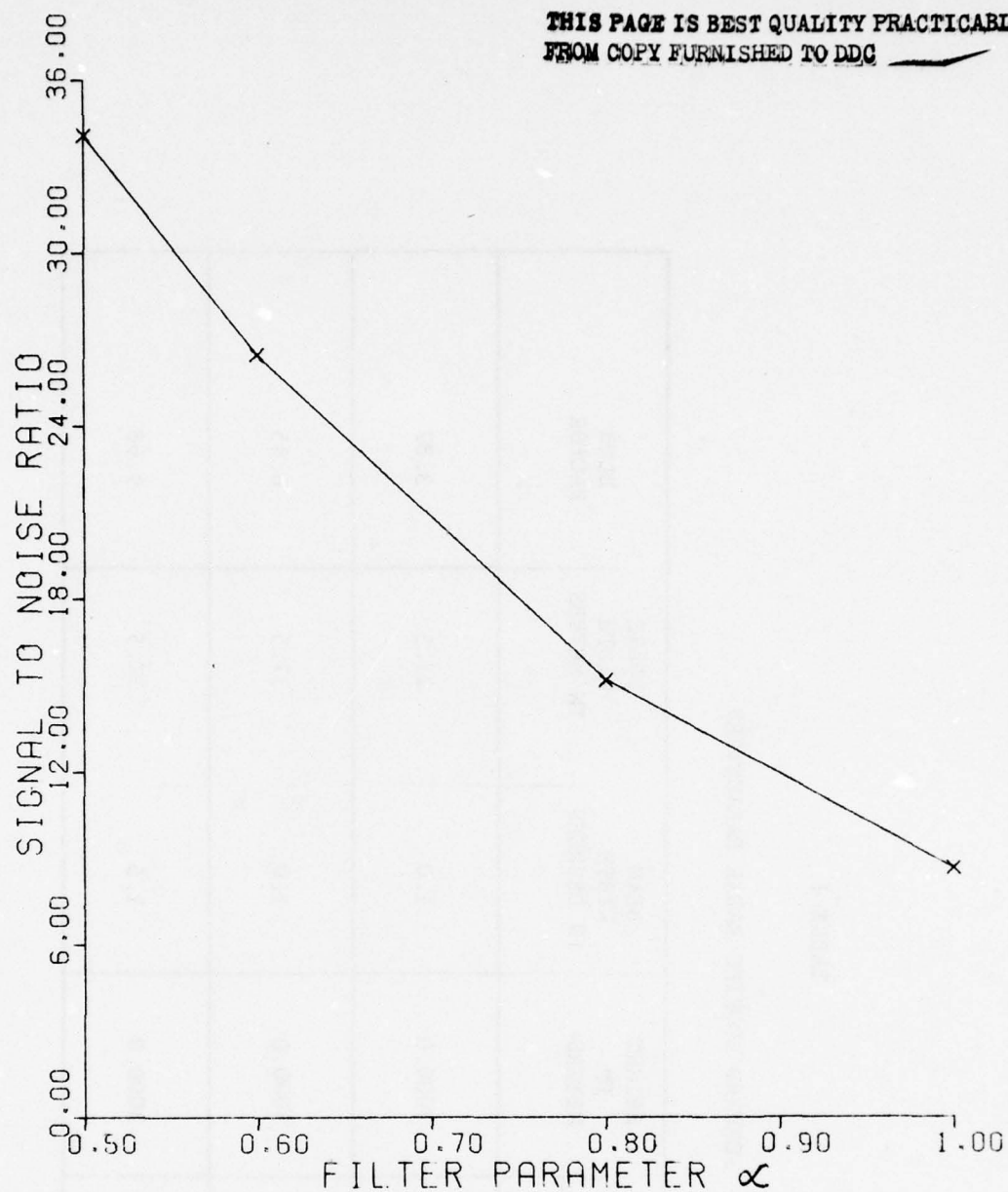


Figure 27: Effect of Fourier domain α -filtering of the FLR-1 image on the signal to noise ratio of the correlation peak

TABLE I
FORWARD LOOKING RADAR PARAMETERS

IMAGE	BEAM ELEVATION ANGLES IN DEGREES		HEIGHT IN METERS	BEAM WIDTH IN DEGREES	PULSE WIDTH IN METERS	BLUR FACTOR
	θ_1	θ_2				
FLR-1	40.0	65.0	3000.0	1.0	22.5	3.87
FLR-2	40.0	65.0	3000.0	1.0	37.5	6.45
FLR-3	40.0	65.0	3000.0	1.5	37.5	9.68

TABLE II

AREA CORRELATION RESULTS

S. N.	REFERENCE IMAGE			IMAGE TO BE CORRELATED			SIGNAL TO NOISE RATIO	PEAK LOCATION
	NAME	FILTER PARAMETER α	SCALING FACTOR S	NAME	FILTER PARAMETER α	ROTATION IN DEGREES		
1.	SLR	1.0	1.0	RADIAL- SLR	1.0	0.0	5.27	(0,0)
2.	SLR	1.0	1.0	FLR-1	1.0	0.0	2.66	(0,0)
3.	SLR	1.0	1.0	FLR-2	1.0	0.0	2.59	(0,0)
4.	SLR	1.0	1.0	FLR-3	1.0	0.0	2.42	(0,0)
5.	SLR	0.5	1.0	FLR-1	1.0	0.0	8.62	(0,0)
6.	SLR	0.5	1.0	FLR-2	1.0	0.0	8.14	(0,0)
7.	SLR	0.5	1.0	FLR-3	1.0	0.0	7.13	(0,0)
8.	SLR	0.5	1.0	FLR-1	1.0	0.5	7.51	(-1,1)
9.	SLR	0.5	1.0	FLR-1	1.0	1.0	6.27	(-2,3)
10.	SLR	0.5	1.0	FLR-1	1.0	2.0	4.86	(-4,6)
11.	SLR	0.5	1.0	FLR-1	1.0	4.0	3.16	(-8,12)
12.	SLR	0.5	0.99	FLR-1	1.0	0.0	7.56	(-1,-1)
13.	SLR	0.5	0.98	FLR-1	1.0	0.0	6.42	(-3,-2)
14.	SLR	0.5	0.96	FLR-1	1.0	0.0	4.53	(5,4)
15.	SLR	0.5	0.98	FLR-1	1.0	0.5	6.10	(-4,0)
16.	SLR	0.5	0.98	FLR-1	1.0	1.0	5.57	(-5,1)
17.	SLR	0.5	0.98	FLR-1	1.0	2.0	4.74	(-7,4)
18.	SLR	0.5	1.0	FLR-1	0.8	0.0	15.16	(0,0)
19.	SLR	0.5	1.0	FLR-1	0.6	0.0	26.45	(0,0)
20.	SLR	0.5	1.0	FLR-1	0.5	0.0	34.06	(0,0)

III. STOCHASTIC IMAGE MODELING AND APPLICATIONS

The simplest stochastic model of an image, at least conceptually, is the joint probability density function. However, for practical reasons (of dimensionality), it is often convenient to work with a two dimensional stochastic difference (or differential) equation representation. State variable models, which convert two dimensional images into a sequence of one dimensional vectors, have been developed and implemented for a variety of image restoration problems by Nahi, Silverman, et. al [1,2]. Ekstrom and Woods [3] have suggested a two dimensional spectral factorization technique for developing non-symmetric half plane (NSHP) models which can be used for recursive image processing applications.

We have demonstrated that the theory of Partial Differential Equations (PDEs) provides a strong framework for studying many problems in image processing [4,5]. Many of these models have been found to be superior to a widely used separable covariance model for images in image restoration applications [6]. These models are divided into three classes according to the classification of PDEs as hyperbolic, parabolic and elliptic equations. It has been shown in [4] that these classes of PDEs could realize different types of correlation functions. Thus, a given correlation function may be best realized (in terms of the minimal order of the PDE) by a particular class of PDEs. For example, certain isotropic correlation functions which fit low resolution images quite well, are best realized by elliptic PDE models.

Our results on image restoration have demonstrated that each class of PDEs leads to a different type of computational algorithm. For example, the hyperbolic equations yield causal vector-recursive, Kalman filtering type algorithms; the parabolic equations yield semi-causal algorithms, i.e.,

algorithms which are causal recursive in one dimension and noncausal in the other; the elliptic equations yield noncausal algorithms. These different structures were shown to give new and different computing architectures as well as performance bounds on the processing technique.

3.1 Causal Models and Hyperbolic PDEs

Consider the operation equation defined on $(0,\infty) \times (0,\infty)$

$$\mathcal{L}_1 v = \frac{\partial^2 v}{\partial x \partial y} + \alpha_1 \frac{\partial v}{\partial x} + \alpha_2 \frac{\partial v}{\partial y} + \alpha_3 v \quad (9)$$

where $v = v(x,y)$. Here \mathcal{L}_1 is a second order hyperbolic PDE operator such that $\mathcal{L}_1 v(x,y) = f(x,y)$ is a well posed initial value problem. A finite difference approximation of this equation gives a discrete random field representation of the type (to be called C1)

$$u_{i,j} = a_1 u_{i-1,j} + a_2 u_{i,j-1} - a_3 u_{i-1,j-1} + \epsilon_{i,j} \quad (10)$$

This is a well known model used for DPCM coding of images. For $a_3 = a_1 a_2$ this equation is an exact realization of the separable covariance model given by

$$R(k,\ell) = E[u_{i,j} u_{i+k,j+\ell}] = \sigma^2 \rho^{|k|+|\ell|},$$

where $E[u_{i,j}] = 0$ and $E[u_{i,j}^2] = \sigma^2$.

The various parameters of (10), are identified as $a_1 = a_2 = \rho$, $a_3 = \rho^2$, $E[\epsilon_{i,j}] = 0$, $E[\epsilon_{i,j} \epsilon_{i+k,j+\ell}] = (1 - \rho^2)^2 \delta_{k,0} \delta_{\ell,0}$ and $\delta_{n,m}$ represents the Kronecker delta function.

3.2 Semicausal Models and Parabolic PDEs

Consider the heat equation operator

$$\mathcal{L}_2 v = v_y - v_{xx} + av \quad (11)$$

This is a second order parabolic PDE operator and leads to a well posed initial value problem in y dimension and well posed boundary value problem in x dimension. A finite discrete approximation of this gives a semicausal representation (SC1), which is causal in j variable and noncausal in i variable, of the form

$$u_{i,k} = \alpha(u_{i-1,j} + u_{i+1,j}) + \gamma u_{i,j-1} + \epsilon_{ij}, \quad (12)$$

where $|\alpha| < \frac{1}{2}$ $|\gamma| < 1$ and $|2\alpha + \gamma| < 1$

This and other semicausal models lead to computationally desirable, the so-called, hybrid algorithms. A hybrid algorithm is a recursive algorithm obtained after transforming each row (or column) of the image by a unitary transform. For such models, it has been shown that a 2-dimensional image can be decomposed into a sequence of one dimensional, independent Markov processes. The statistics of certain semicausal models have been shown to fit high resolution images quite well [4,6].

3.3 Noncausal Models and Elliptic PDEs

Consider the well known Poisson operator equation

$$\mathcal{L}_3 v = v_{xx} + v_{yy} + av \quad (13)$$

This is a boundary value elliptic PDE. Such equations have been shown to yield noncausal stochastic image models and have shown to fit, quite well, satellite and other remotely sensed images, which have nearly isotropic covariance functions. Noncausal models have also been useful for representing images with separable covariance functions [4,6]. The advantage of such representations is that often, they yield computationally fast Karhunen Loeve (KL) expansions of image data and have proven useful in restoration and data compression of images.

3.4 Application to Rdar Image Area Correlation Techniques

For the sake of clarity in understanding, we shall work here with one dimensional images defined over an interval $[-a, a]$. Correspondingly the area correlation is defined as

$$c(x) = \frac{1}{2a} \int_{-a}^a I_1(\xi + x) I_2(\xi) d\xi \quad (14a)$$

In practice the reference image I_1 could be considered as representing the terrain features very accurately and I_2 a blurred image of the terrain given as

$$I_2(x) = \int_{-a}^a h(x - \xi) I_1(\xi) d\xi, \quad (14b)$$

where $h(x)$ is the point spread function of the imaging optics. As a first approximation $h(x)$ is assumed to be spatially invariant. Extension to spatially variant case is possible (although the computational complexity may increase). Combining (14a) and (14b) we get

$$c(x) = \frac{1}{2}a \int_{-a}^a \int_{-a}^a h(\xi - \xi') I_1(\xi') I_1(x + \xi) d\xi d\xi' \quad (14c)$$

For evaluation of an area correlation system, generally, the first two moments of $c(x)$ are needed. From above these are obtained, assuming I_1 to be a stationary process whose autocorrelation is R_{11} , as

$$m_1(x) \triangleq E[c(x)] = \frac{1}{2}a \iint h(\xi - \xi') R_{11}(\xi - \xi' + x) d\xi d\xi' \quad (15a)$$

$$m_2(x) = E[c^2(x)] = \frac{1}{2}a \iiint \int h(\xi - \xi') h(\eta - \eta') E[I_1(\xi') I_1(x + \xi) I_1(\eta') I_1(x + \eta)] \cdot d\xi d\xi' d\eta d\eta' \quad (15b)$$

Equations (15a) and (15b) can be evaluated, at least in principle, if the second and fourth order statistics of the random process I_1 are known. Measurement of such statistics from available data is impractical even when stationarity and ergodicity assumptions are made. This is because in (15b), for an N point discretization of $I_1(x)$, at least N^3 coefficients for the fourth order expectation will be required. For two dimensional images, the dimensionality will be $O(N^6)$. Hence, it is desirable to have a different stochastic representation for I_1 so that all the statistical parameters can be calculated from it. One way is to determine a stochastic PDE representation of the two dimensional image $I_1(x,y)$ and determine all the statistics from that model. This approach would be the 2 dimensional equivalent of calculation of, say, the autocorrelation function of a one dimensional random process from its stochastic, ordinary differential equation model. The difference would be that one would have to solve PDEs for two dimensional variables.

IV. REAL-TIME RF SIMULATION OF RE-ENTRY VEHICLES

The availability of an image model is particularly useful in real time simulation of radar imaging systems. For example, in a hardware in the loop simulation of a terminal guidance system at the Advanced Simulation Center of U.S. MIRADCOM, Redstone Arsenal, Alabama, it is planned to generate, in real time, image signals as shown in Fig. 28. Here, the re-entry vehicle (RV) flight hardware (Radar scanning antenna, the radar receiver electronics, and the correlator unit) is mounted at one end of a chamber and the scanning antenna (i.e., the FLR) is allowed to rotate, as it operates in the real environment. This radar antenna scans a large array of antennas located at the other end of the RFSS chamber. Digital image signals generated by a digital computer are converted to analog video signals and are put on Radio Frequency (RF) carrier pulses for transmission from the array. By a sophisticated computer controlled switching method, signals are radiated from the array such that they are synchronous with the scanning antenna position. The signal power levels and array position control are fine enough to simulate the real time radar return signals received by the RV. The reference and the live FLR images are updated in real time as the trajectory of the RV changes. A sequence of reference images is known in advance at few fixed points on the trajectory. The reference image at any point is prepared off line and the relevant images stored in advance for signal generation.

Fig. 29 shows a more detailed design architecture developed by the principal investigator during an LRCP research effort for a real time hardware in the loop simulation (at U.S. MIRADCOM) of an area-correlation system. The principal advantage of these simulations is that by including complex hardware in the simulation loop, realistic flight test data can be obtained for system evaluation. This will of course minimize the number of actual test flights needed and will therefore reduce test costs.

THIS PAGE IS BEST QUALITY PRACTICABLE
FROM COPY FURNISHED TO DDC

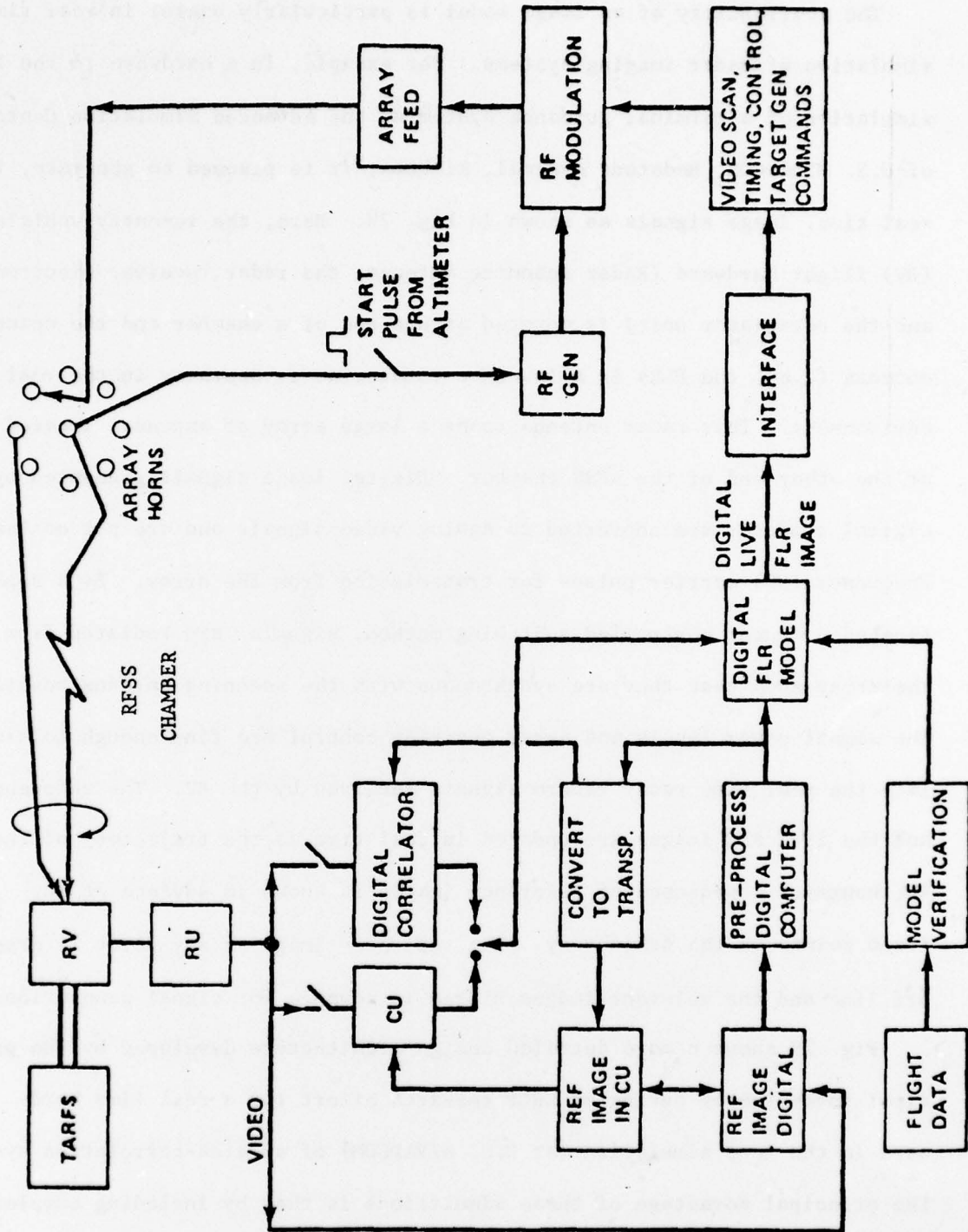


FIGURE 28 OVERVIEW OF REAL TIME HARDWARE IN THE LOOP SIMULATION OF AN AREA CORRELATION GUIDANCE SYSTEM

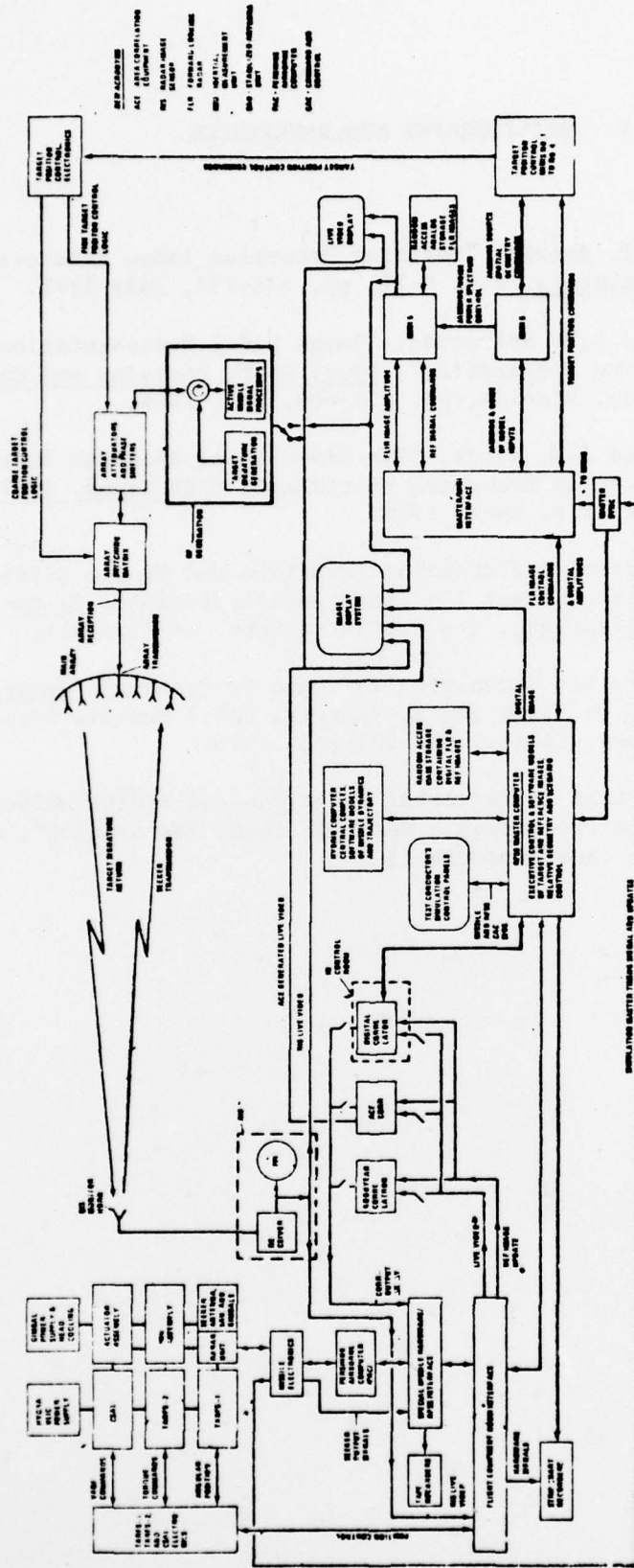


FIGURE 29 DETAIL ARCHITECTURE OF REAL TIME RV SIMULATION AT U.S. MIRADCOM

V. BIBLIOGRAPHY AND REFERENCES

1. N.E. Nahi and T. Assefi, "Bayesian Recursive Image Enhancement", IEEE Trans. Computers, vol. C-21, pp. 734-737, July 1972.
2. M.S. Murphy and L.M. Silverman, "Image Model Representation and Line by Line Recursive Restoration", Proc. Conf. Decision and Control, Clearwater Beach, Florida, pp. 601-606, Dec. 1976.
3. M.P. Ekstrom and J.W. Woods, "Two Dimensional Spectral Factorization with Applications in Recursive Filtering", IEEE Trans. ASSP, vol. ASSP-24, pp. 115-128, April 1976.
4. A.K. Jain, "Partial Differential Equations and Finite Differences in Image Processing, Part I - Image Representation", J. Optimization Theory and Applications, (to appear in Sept. 1977 issue).
5. A.K. Jain, "Some New Techniques in Image Processing", Image Science Mathematics, (C.O. Wilde and E. Barrett, Eds.) Western Periodicals Co., N. Hollywood, Calif., pp. 201-223, 1976.
6. A.K. Jain, "Partial Differential Equations and Finite Difference Methods in Image Processing - Part II: Image Restoration", submitted for publication (see Appendix I)

APPLICATION OF PARTIAL DIFFERENTIAL EQUATIONS IN IMAGE RESTORATION

by

Anil K. Jain
Jaswant R. JainDepartment of Electrical Engineering
State University of New York at Buffalo
Bell Hall, Amherst Campus
Buffalo, New York 14260ABSTRACT

Stochastic representation of discrete images by partial differential equations proposed earlier in [1] is used for filtering of noisy images. Comparisons among various representations and their relative effectiveness in modeling the actual statistics of the images is shown by examples. Certain image decompositions resulting in fast filtering algorithms are given. The results are also compared with spatial averaging and Fourier domain Wiener filters. Results show superiority of noncausal and semicausal models over causal and/or separable covariance models.

I. INTRODUCTION

In an earlier paper [1] image representation by partial differential equations (PDEs) was considered. It was shown that corresponding to the PDE classification of hyperbolic, parabolic, and elliptic systems, three different stochastic representations viz., causal, semicausal, and noncausal representations are realized. These representations have different spatial structures and are realizations of different type of covariance functions. For example, certain elliptic equations can realize certain isotropic covariance functions which cannot be realized by hyperbolic or parabolic equations. On the other hand certain covariance functions could be realized by all the three classes of representations. Use of PDEs directly for image representation bypasses the difficult problem of two dimensional spectral factorization. The experimental results of [1,2] have shown that the covariance functions realized by some of the PDEs approximate the actual covariance of different image data better than the commonly used covariance function models for those image data.

In this paper we consider the problem of linear filtering of noisy images represented by different PDE models. It is shown that the causal, semicausal, and noncausal models give rise to recursive, hybrid or semi-recursive, and transform domain or nonrecursive filtering algorithms. Recursive filtering for images has been considered earlier by many researchers [3-7]. Typically in these approaches, one insists on a causal image representation e.g., state variable or two dimensional autoregressive models, such that recursive filtering equations of Kalman and Bucy, or equivalently, those of Aasnaes and Kailath [8] are applicable. By hybrid or semirecursive filtering we mean a filtering method which is non-recursive in one of the image dimensions and is recursive in the other. Algorithms of this type include those vector recursive algorithms where the state variable vector contains an entire

column (or row) of the image, and have been considered by Jain [9], Murphy and Silverman [10] and others [11, 12]. Nonrecursive or transform domain algorithms arise quite naturally for noncausal models and lead to smoothing equations very similar to discrete Fourier Transform (DFT) domain Wiener filters. Similar algorithms have been studied previously in [19].

Although some of the image models (and their associated filter equations) considered here have been studied earlier [9,13,19], this paper reconsiders these as well as some new models in the more general framework of PDEs. This has several advantages. First, the well developed theory of PDEs offers many analytical answers to problems related to stability, stationarity, performance bounds, etc. Second, the different existing numerical methods for solving PDEs hold promising possibilities for implementing filter solutions. Finally, the PDE theory lends insight into certain filtering phenomena. An example of this is shown in section 5 to explain the performance of a spatial averaging filter. Several filtering experiments on actual images and comparisons of different models, old and new, exemplify the utility of our approach.

In section 2 we briefly review the results of [1] that are used here. Specifically, the different models identified in [1] are summarized and some notation is established. In section 3, 4 and 5 the filtering algorithms associated with the causal, semi-causal, and noncausal models respectively, are described. Filtering experiments on four different images have been performed. In section 6, the results of these experiments and their mutual comparisons as well as with standard Fourier domain Wiener filtering techniques are discussed. Conclusions and possible extensions of this work are given in section 7.

2. PDE IMAGE MODELS

Stochastic PDEs have been studied earlier for various applications [14-18]. In a recent paper Jain [1] has studied the possibilities of modeling actual image data by PDEs and many different models have been suggested. Table I summarizes some of those models which we will be studying here for filtering applications. We start with a PDE operator $L(\partial/\partial x, \partial/\partial y)$ and approximate it by discrete operator $D(\mathbf{u}_1, \mathbf{u}_2)$, obtained by a suitably chosen finite difference method. Then we assume an image representation of the form

$$D[\mathbf{u}_{1,j}] = \mathbf{e}_{1,j},$$

where $\mathbf{u}_{1,j}$ represents the (relative) brightness of the zero mean unit variance image at the point $(1,j)$ for $-\infty \leq j \leq \infty$ and $\mathbf{e}_{1,j}$ is a two dimensional zero mean discrete white noise or some sort of moving average process with absolutely continuous spectral density function. Clearly, \mathbf{u}_1 and \mathbf{u}_2 in $D(\mathbf{u}_1, \mathbf{u}_2)$ can also be chosen to be the two dimensional \hat{z} -transform variables. If we denote $S_{\mathbf{e}}(\mathbf{u}_1, \mathbf{u}_2)$ to be the spectral density function of

Presented at the IEEE Computer Society Conference on Pattern Recognition and Image Processing, Rensselaer Polytechnic Institute, Troy, N.Y., June 6-8, 1977.

THIS PAGE IS BEST QUALITY PRACTICABLE FROM GPOFF FURNISHED TO DDG

$\{e_j\}$ for $a_1 = \exp(jw_1)$, $a_2 = \exp(jw_2)$, then the spectral density function of $\{u_{i,j}\}$ is given by

$$S_u(a_1, a_2) = S_e(a_1, a_2) / (D(a_1, a_2) \cdot D(a_1^{-1}, a_2^{-1})).$$

The covariance function of $\{u_{i,j}\}$ is obtained quite easily by the Fourier inverse of $S_u(e^{jw_1}, e^{jw_2})$, which could be accomplished by a suitable FFT algorithm. Table I lists the forms of S_e chosen for various models. The values of different parameters identified for these models, for a 256x256 Girl image, are listed in Table II. Here σ^2 represents $E\{e_j^2\}$ and is the value of $S_e(0,0)$. Table I also shows the spatial structure of the different models arising from a finite difference approximation of the operator L . Here, if $u_{i,j}$ corresponds to the point marked A, then the spatial structure shows all other points that are used directly in the prediction of A. The stability of various models and their stationarity (asymptotically) is assured by imposing restrictions on the model parameters which are consistent with the well posedness of the original PDEs. The parameters of Table II satisfy those restrictions and realize stationary fields. Parameters for some other images and related details can be found in [1,2].

We will consider the simplest filtering problem where the observations are given as

$$y_{i,j} = u_{i,j} + n_{i,j}, \quad (1)$$

where (i,j) belongs to a set I , of integer pairs and $\{n_{i,j}\}_2$ is a zero mean white Gaussian noise of variance σ_n^2 . The set I will be suitably defined for different image models as we proceed in the paper. We would be interested in the various predictors, on-line filters and smoothers of $u_{i,j}$, given the observations of (1). It should be noted that the models are stationary for infinite images. To apply them for restoration of finite size images certain initial and/or boundary conditions on the models will have to be specified. If stationarity is to be retained, the boundary conditions should be consistent with the covariance function realized by the model. In practice, these consistent specifications may be difficult at times and one may, instead, settle for a nonstationary model which is asymptotically stationary, by assuming a more convenient model for the boundary variables. In fact we will see that, implementation wise, some of the simplest algorithms are obtained for nonstationary (but spatially invariant) models whose boundary conditions are deterministic. This would result in suboptimality, which depends on image size, and may not always be significant compared to the error in modeling. Throughout the paper we will attempt to point out such optimality vs feasibility tradeoffs.

3. CAUSAL MODELS

Causal models considered here result from a hyperbolic system of PDEs and have spatial structure of the form

$$u_{i,j} = a_1 u_{i-1,j} + a_2 u_{i,j-1} - a_3 u_{i-1,j-1} + e_{i,j}, \quad (2)$$

For $a_3 = a_1 a_2$ this results in an often used separable covariance function. Such a model has been considered by Habibi [6] for recursive filtering, but the equations developed there have been shown to be in error by Strintzis [7]. Recently Bary, et al [17] have developed some asymptotic recursive filters for such models. More recently Wong [16] has mentioned that two dimensional recursive filter for the continuous equivalent of this model exists and that the filtering equations are rather complicated. Here we consider the recursive filtering equations for the discrete model of (2) and show that these equations may be obtained

from a set of one dimensional vector recursive equations.

If u_j denotes the $N \times 1$ column vector of an $N \times M$ image then (2) can be written in vector form as

$$L_1 u_j = L_2 u_{j-1} + e_j + b_j, \quad 1 \leq j \leq M, \quad (3)$$

where L_1 and L_2 are nonsingular lower triangular Toeplitz matrices and b_j are $N \times 1$ vectors containing initial conditions. If b_1 is orthogonal to u_{j-1} and e_j and if it is a white noise process (for $a_3 = a_1 a_2$ this is true) and if we define $f_j = e_j + b_j$ then (3) becomes a vector Markov process

$$u_j = L_1^{-1} L_2 u_{j-1} + f_j. \quad (4)$$

The observations of (1) can be written in a vector form as

$$y_j = u_j + n_j. \quad (5)$$

Various vector recursive filtering equations can now be written quite straightforwardly. For example, if a column vector is scanned at a time and the previously scanned vectors are used to predict the next column vector, then the Kalman filtering equation for one step predictor can be written as

$$\hat{u}_{j+1} = L_1^{-1} L_2 \hat{u}_j + G_j (y_j - \hat{u}_j), \quad \hat{u}_0 = 0, \quad (6)$$

where G_j is Kalman gain matrix that is obtained by solving an associated Riccati equation. For a true two dimensional recursive filter suppose the image is a scalar scanned image, e.g., raster scanning, say from top to bottom (along i) and left to right (along j). For such a scanning the one step predictor, $u_{i+1,j}$, is defined as the best linear estimate of $u_{i+1,j}$ given the observations up to the previous scan point i.e., $y_{i,j}$. The solution of such a recursive filter, results in a one step predictor given by

$$\hat{u}_{i+1,j} = x_j^{i+1} \quad (7)$$

where x_j^i is a "state vector" for the estimates at scanner position (i,j) and satisfies

$$x_j^{i+1} = x_j^i + h_j^i v_{i,j}^i; \quad x_j^0 = \hat{u}_j, \quad 0 \leq i \leq N-1 \quad (8)$$

$$v_{i,j}^i = y_{i,j} - x_j^{i-1}(i) \quad (9)$$

Here x_j^i is a $N \times 1$ column vector representing the best estimate of j th column vector u_j given observations only up to $y_{i,j}$; $v_{i,j}^i$ is the scalar scanner innovations process, and h_j^i is another gain vector and is a function of G_j of (6). Note that the initial condition of (8) requires first solving the vector recursive filter equation (6) up to step j . Hence, we have to solve two sets of vector equations i.e., (6) and (8) one in the horizontal (j) direction and the other in the vertical (i) direction to obtain a two dimensional scanner recursive filter. The major computational effort is in the solution of the Riccati equation for G_j and h_j^i . For large image size G_j and h_j^i can be replaced by their steady state values and the resulting filter equations then require about $O(N^2)$ operations per vector step (or a total of about $O(N^3)$ operations). Further simplifications are possible by noting that G_j becomes a Toeplitz matrix when $i,j \rightarrow \infty$ and (6) reduces to convolution operations. For the separable model (i.e. for $a_3 = a_1 a_2$) an iterative, smoothing filter is also possible. If we write (1) in matrix form

$$U = Y + n, \quad (10)$$

and if $E[n_{i,j} \cdot n_{k,\ell}] = \sigma_n^2 \cdot \delta_{i,k} \cdot \delta_{j,\ell}$ then the

smoothed estimate of the image using CI model can be found by iterative solution of the following equation in the sine transform domain [2]*

$$U_{k+1} + \frac{\sigma_n^2}{\beta^4} Q U_{k+1} Q = Y - B_k, U_0 = 0, \quad (11)$$

where

$$B_k = \frac{\sigma_n^2}{\beta} a^2 D U_k D + \frac{\sigma_n^2}{\beta^2} a (DU_k Q + QU_k D), \quad (12)$$

$$a = \rho^2 / (1 - \rho^2),$$

and Q and D are NxN matrices defined by

$$q_{i,j} = \begin{cases} 1 & , i=j \\ -\alpha & , |i-j|=1 \\ 0 & , \text{otherwise,} \end{cases} \quad (13)$$

$$d_{1,1} = d_{N,N} = 1, d_{1,j} = 0, \text{ otherwise, where}$$

$\alpha = \rho / (1 + \rho^2)$. The reason we opt to solve (11) and (12) in sine transform domain is that the sine transform diagonalises the matrices Q and D and then they could be solved as set of N scalar independent equations, thus resulting in computational savings. Details of derivations will be given elsewhere.

4. SEMICAUSAL MODELS

If u_j denotes the Nx1 column vector of an NxN image then, the semicausal models SC1 and SC2 given in Table I can be written as

$$Qu_j = Pu_{j-1} + \epsilon_j + b_j, \quad 1 \leq j \leq N \quad (14)$$

where Q is an NxN symmetric, tridiagonal, Toeplitz, matrix defined in (13); $P = \gamma I$ for SC1 and $P = \rho Q$ for SC2 models; and b_j is a Nx1 column vector consisting of only boundary values identified as

$$b_j = \begin{cases} \alpha \cdot (u_{0,j}, 0, \dots, 0, u_{N+1,j})^T, & \text{for SC1,} \\ \alpha \cdot (u_{0,j} - \rho u_{0,j-1}, 0, \dots, u_{N+1,j} - \rho u_{N+1,j-1})^T, & \text{for SC2.} \end{cases}$$

The statistics of ϵ_j could then be identified as

$$E[\epsilon_j] = 0, \quad \text{for SC1 \& SC2,}$$

and

$$E[\epsilon_j \cdot \epsilon_k^T] = \begin{cases} \beta^2 I \delta_{j,k}, & \text{for SC1} \\ \beta^2 Q \delta_{j,k}, & \text{for SC2} \end{cases} \quad (15)$$

The semicausal structure of (14) is evident by noting the noncausality of any element $u_{i,j}$ of the image in the i variable and its causality in j variable. Any attempt to reindex these equations as recursive in the i variable would result in unstable causal systems and will no longer represent (asymptotically) stationary random fields [9].

Letting b_j contain arbitrary boundary values, random or deterministic, we define two processes u_j^o and u_j^b as

$$Qu_j^o = Pu_{j-1}^o + \epsilon_j, \quad u_0^o = 0, \quad (16)$$

$$\text{and} \quad Qu_j^b = Pu_{j-1}^b + b_j, \quad u_0^b = u_0. \quad (17)$$

*The sine transform is related to the discrete Fourier transform and has a fast implementation algorithm similar to FFT algorithm.

For a nonsingular matrix Q, (14) will have a unique solution. From this uniqueness of u_j and linearity of (14) it follows from (16) and (17) that u_j has the stochastic decomposition

$$u_j = u_j^o + u_j^b, \quad 1 \leq j \leq N. \quad (18)$$

The vector u_j^b is called the boundary response of u_j and is completely determined by the initial and the boundary values of the image. This decomposition would be orthogonal if $\{\epsilon_j\}$ and $\{b_j\}$ are uncorrelated sequences i.e.,

$$E[\epsilon_j b_k^T] = 0, \quad \forall j, k$$

The above condition is always satisfied for the SC2 model. Note that (16) is now a nonstationary Markov process starting with a zero initial state. Using (18) in eqn. (5) the observations can be written as

$$y_j^o = y_j^o + u_j^b \quad (19)$$

where

$$y_j^o = u_j^o + \eta_j. \quad (20)$$

Now noting the fact that the discrete sine transform Ψ diagonalises any tridiagonal symmetric Toeplitz matrix, such as P and Q the vector equations (16), (17), (19) and (20) can be converted into scalar decoupled set of causal Markov representations by taking their sine transform. The Kalman filtering equations for the resulting equations in the Sine transform domain are given quite easily as follows.

One Step predictor

$$\hat{v}_{j+1} = c \hat{v}_j + c \hat{\gamma}_j f_j (\epsilon_j - \hat{v}_j) / \sigma_n^2, \quad \hat{v}_0 = 0 \quad (21)$$

$$\hat{\gamma}_{j+1} = c^2 \hat{\gamma}_j f_j + d^2 \sigma^2, \quad \hat{\gamma}_0 = 0$$

$$f_j = (1 + \hat{\gamma}_j / \sigma_n^2)^{-1}$$

$$\sigma^2(i) = E[\epsilon_j^2(i)] \quad 1 \leq j \leq N.$$

On-line filter

$$\bar{v}_j = \hat{v}_j + \hat{\gamma}_j f_j (\epsilon_j - \hat{v}_j) / \sigma_n^2 \quad (22)$$

Interpolator (Smoother)

$$v_j^* = \hat{\gamma}_j \omega_j + \bar{v}_j \quad (23)$$

$$\omega_j = c f_j \omega_{j+1} + f_j (\epsilon_j - \hat{v}_j) / \sigma_n^2, \quad \omega_{N+1} = 0$$

where,

$$z_j \triangleq \Psi y_j^o, \quad v_j \triangleq \Psi u_j, \quad \epsilon_j \triangleq \Psi \epsilon_j,$$

$$c(i) = \gamma / \lambda_i \quad \text{and} \quad d(i) = \lambda_i^{-1} \quad \text{for SC1,}$$

$$c(i) = \rho \quad \text{and} \quad d(i) = \lambda_i^{-1} \quad \text{for SC2.}$$

All the above equations for filters are decoupled in the variable i and can be solved independently for each i . (The subscript i has been omitted for notational simplicity). From these the spatial domain image estimates are given by inverse unitary transformation ($\Psi^{-1} = \Psi^T = \Psi$), i.e.

$$u_j^* = u_j^{o*} + u_j^b = \Psi v_j^* + u_j^b, \text{ etc.}$$

The semicausal model recursive algorithm is, very simply, as follows. From the given boundary values (or

their estimates) first calculate u^b , and determine the modified observations y_i^0 . Then transform y_i^0 by the (first) Sine transform and solve the desired recursive filter equations. The inverse transformation of the recursive filter estimate and adding u^b gives the desired filtered image vector. For details of SC2 model see [9].

5. NONCAUSAL MODELS

From the spatial structures of the noncausal models NC1, NC2 and NC3 (see Table 1) it can be seen that they are nonrecursive in both the indices i and j . Any attempt to reindex them so as to yield a recursive relation in either of the indices would result in an unstable system. Let U be an $N \times N$ image matrix and \bar{U} be an $N^2 \times 1$ vector obtained by the lexicographic ordering of U , then the noncausal models can be written in the form

$$J \bar{U} = \bar{e} + \bar{B} \quad (24)$$

where J is an $N^2 \times N^2$ matrix, \bar{e} is the $N^2 \times 1$ vector corresponding to the matrix e containing $\{e_{i,j}\}$, and \bar{B} is a $N^2 \times 1$ vector whose entries depend only on the boundary values. From (24) one gets the decomposition

$$\bar{U} = \bar{U}^0 + \bar{U}^b \text{ or } U = U^0 + U^b \quad (25)$$

$$\text{where } \bar{U}^0 = J^{-1} \bar{e}, \quad \bar{U}^b = J^{-1} \bar{B}. \quad (26)$$

Note that \bar{U}^b is completely determined from the boundary values and is called the boundary response. Let

$$R_e \triangleq E[\bar{e} \bar{e}^T] = \beta^2 \cdot \Sigma, \quad (27)$$

then from (26) and (27) the covariance matrix of \bar{U}^0 is obtained as

$$R_{\bar{U}^0} \triangleq E[\bar{U}^0 \bar{U}^{0T}] = \beta^2 J^{-1} \Sigma J^{-1}. \quad (28)$$

The structures of the matrices J and Σ resulting from the PDEs considered is such that the Kronecker product $\Psi \otimes \Psi$ of the Sine transform Ψ contains all the eigenvectors of J and Σ for NC1 and NC3 models (For NC2 model this is still a good approximation). Therefore $\Psi \otimes \Psi$ becomes the Karhunen Loeve (KL) transform of \bar{U}^0 . Hence, if

$$\bar{V}^0 = (\Psi \otimes \Psi) \bar{U}^0 \text{ or } V^0 = \Psi V^0 \Psi, \quad (29)$$

then V^0 is the K-L transformations of U^0 and its elements will be uncorrelated. As before, the observations can also be decomposed to give

$$Y = Y^0 + U^b, \quad (30)$$

$$\text{where } Y^0 = U^0 + \eta. \quad (31)$$

Now if the boundary values (or equivalently U^b) were deterministic we can obtain the Wiener filter equations from (25) and (31) in KL transform (Ψ) domain as N^2 decoupled scalar equations and are found to be

$$v_{i,j}^* = \frac{\beta^2 a_{i,j} + \sigma_n^2 \cdot l_{i,j} \cdot c_{i,j}/k_{i,j}}{\beta^2 + \sigma_n^2 \cdot l_{i,j}^2/k_{i,j}} \quad 1 \leq i, j \leq N.$$

where $V = \Psi U \Psi$, $Z = \Psi Y \Psi$, $C = \Psi B \Psi$, $\sigma_n^2 = E[\eta_{i,j}^2]$, $l_{i,j}$ and $k_{i,j}$ are the N^2 eigenvalues of J and Σ respectively. The optimal smoothed estimate of the image is then found by inverse sine transform of V^* , i.e.,

$$U^* = \Psi V^* \Psi.$$

In practice the boundary values may not be determinis-

tic. In that case, these are estimated first and are used to determine U^b . This will make our scheme slightly suboptimal although its significance decreases as the image size increases. See [19] for an analysis of boundary effects.

6. EXAMPLES AND DISCUSSION

The filtering techniques discussed in the previous sections were implemented on four 65×65 blocks of four 256×256 images corrupted by white Gaussian noise. The Signal to Noise ratio (S/N) values of 1, 2, and 5 were used. This ratio is defined as

$$S/N = \frac{\text{Standard deviation of the signal}}{\text{Standard deviation of the noise}}$$

The various models are compared mutually as well as with their corresponding Fourier domain Wiener filters and spatial averaging filters. The spatial averaging filter averages each pixel with the nearest four points, i.e.,

$$u_{i,j}^* = \frac{1}{4} [y_{i,j} + y_{i+1,j} + y_{i-1,j} + y_{i,j+1} + y_{i,j-1}].$$

For causal model C1 the iterative solution of (11) and (12) was used. For solving semicausal and noncausal filter equations the boundary values were first estimated separately. For these models the size of the image block U was taken to be 63×63 and with boundaries the total block size becomes 65×65 . The four boundary vectors were estimated independently using one dimensional Fourier-Wiener filter and first order Markov statistics.

These boundary estimates were used (instead of the actual boundary values) in computing the boundary response functions. For NC2 model two boundaries on each side of the image are needed and we have assumed the outer most boundaries to be zero.

Tables III, IV, and V show the comparisons among the performance of various filters for S/N of 1, 2 and 5 respectively. The C1, SC2 and NC3, all correspond to the separable covariance model and hence their results differ only in terms of the requirements of knowledge of the boundaries. As expected, their performance is quite close and the difference depends on how good are the boundary estimates. Their poor performance for the blocks of the MOON and ERTS images was found to be due to the fact that the one step correlation parameter, ρ , for these blocks was significantly different from the one measured for the larger 256×256 images. On the other hand, the other models (SC1, NC1 and NC2) perform relatively very well on these blocks. This implies that the latter models are much more stable, i.e., they are relatively insensitive to the local changes in statistics.

The superior performance of the NC1 and SC1 models is evident from their filter performances. Except for the couple image block the performance of NC1 is the best in almost all the cases. In most cases NC2 performs better than the separable models but is poorer than NC1 and SC1 models. The superior performance of these models may be attributed to the superiority of their fitting to the image statistics.

The simple, adhoc, Spatial Averaging filter performs surprisingly well, especially for moderate signal to noise ratios. Note that it performs better than the C1, SC2 and NC3 models. This can be explained by the fact that the transfer function of the spatial averaging filter is a fairly good approximation of the Fourier-Wiener filter corresponding to the NC1 model, which as we have seen here, is a very good model for filtering of images. Tables III to V also show that almost all the filters perform somewhat better than their corresponding Fourier domain Wiener filters. This is because for finite size images, the Fourier domain samples (of observations and the original data)

are correlated and the corresponding Wiener filter is suboptimal [20]. The semicausal and noncausal filter are also suboptimal whenever the boundary values are not known exactly. However, this suboptimality is less significant than the Fourier domain suboptimality.

Fig. 1 shows some of the images resulting from the application of the foregoing filters. The performance differences due to different filters were also evident on a visual display.

7. CONCLUSIONS

In conclusion, it was demonstrated that different PDE classes yield different filter structures and also different filter performances. Many of these models offer substantial advantages, both in terms of computational complexity as well as filter performance, over the conventional, separable image covariance models. More general PDE models may be used to achieve even better results. Also, these models may be used for other two dimensional signal processing applications such as data compression, detection, synthesis, etc. [21]. Inevitably, in all these applications numerical methods for solving PDEs will play a major role.

REFERENCES

- [1] A.K. Jain, "Partial Differential Equations and Finite Differences in Image Processing, Part I-Image Representation," J. Optimization Theory and Appl., (to appear in 1977).
- [2] A.K. Jain and J.R. Jain, "Partial Differential Equations and Finite Differences in Image Processing," Dept. of Elect. Engg., Tech. Rep. AJ-76-003, State Univ. of New York at Buffalo, May 1976.
- [3] N.E. Nahi and T. Assefi, "Bayesian Recursive Image Estimation," IEEE Trans. Computers, Vol. C-21, pp. 734-737, July, 1972.
- [4] N.E. Nahi and C.A. Franco, "Recursive Image Enhancement - Vector Processing," IEEE Trans. Communications, Vol. COM-21, pp. 305-311, March, 1973.
- [5] A.O. Aboutalib and L.M. Silverman, "Restoration of Motion Degraded Images," IEEE Trans. Circuits and Systems, Vol. CAS-22, pp. 278-286, March, 1975.
- [6] A. Habibi, "Two Dimensional Bayesian Estimate of Images," Proc. IEEE, Vol. 60, pp. 878-883, July, 1972.
- [7] M.G. Strintzis, "Comments on Two Dimensional Bayesian Estimate of Images," Proc. IEEE, Vol. 64, pp. 1255-1257, August, 1976.
- [8] H.B. Aasnaes and T. Kailath, "An Innovations Approach to Least Squares Estimation-Part VII: Applications of Vector Autoregressive Moving Average Models," IEEE Trans. Aut. Control, Vol. AC-18, pp. 601-608, December 1973.
- [9] A.K. Jain, "A Semicausal Model for Recursive Filtering of Two Dimensional Images," (to appear in IEEE Trans. Computers, 1977), also see Proc. Conf. Decision and Control, Houston, Texas, Dec., 1975.
- [10] M.S. Murphy and L.M. Silverman, "Image Model Representation and Line by Line Recursive Restoration," Proc. Conf. Decision and Control, Clearwater Beach, Florida, pp. 601-606, Dec., 1976.
- [11] J.W. Woods, "Markov Image Modeling," Proc. Conf. Decision and Control, Clearwater Beach, Florida, pp. 596-600, Dec., 1976.
- [12] E. Wong, "Detection and Filtering for Two Dimensional Random Fields," Proc. Conf. Decision and Control, Clearwater Beach, Florida, pp. 591-595, Dec., 1976.
- [13] A.K. Jain and E. Angel, "Image Restoration, Modeling and Reduction of Dimensionality," IEEE Trans. Computers, Vol. C-23, No. 5, pp. 470-476, May, 1974.
- [14] P. Whittle, "On Stationary Processes in the Plane," Biometrika, Vol. 41, pp. 434-449, 1954.
- [15] V. Heine, "Models for Two Dimensional Stationary Stochastic Processes," Biometrika, Vol. 42, pp. 170-178, 1955.
- [16] E. Wong, "Recursive Filtering for Two Dimensional Random Fields," IEEE Trans. Inf. Theory, Vol. IT-21, pp. 84-86, Jan., 1975.
- [17] P.E. Barry, R. Gran and C.R. Waters, "Two Dimensional Filtering: A State Estimator Approach," Proc. Conf. Decision and Control, Clearwater Beach, Florida, pp. 613-618, Dec., 1976.
- [18] E. Angel and A.K. Jain, "Frame to Frame Restoration of Diffusion Images (to appear), also see "Filtering of Multidimensional Diffusion Processes," 6th Asilomar Conf., Pacific Grove, Asilomar, California, Nov., 1972.
- [19] A.K. Jain, "A Fast Karhunen-Loeve Transform for Recursive Filtering of Images Corrupted by White and Colored Noise," (to appear in IEEE Trans. Computers).
- [20] A.K. Jain and R. Padgug, "Fast Restoration of Finite Objects Degraded by Finite PSF," (to appear in J. Comp. Physics).
- [21] A.K. Jain, "Some New Techniques in Image Processing", in Image Science Mathematics (C. Wilde and E. Barrett, Editors), Proceedings Symp. on Current Mathematical Problems in Image Science, Naval Post Grad. School, pp. 201-223, Nov., 1976.



a) Original



b) Noisy



c) Separable Model F-W Filter



d) NCI Model F-W Filter



e) SCI Model Filter



f) NCI Model Filter

Fig. 1: SMOOTHING OF A 64 x 64 BLOCK OF THE GIRL IMAGE

TABLE 1

SUMMARY OF SOME PDE MODELS AND THEIR DISCRETE APPROXIMATIONS $D[U] = \epsilon$ USED FOR IMAGE MODELLING.


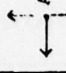




S. N.	MODEL	PDE OPERATOR	DISCRETE OPERATOR $D(z_1^{-1}, z_2^{-1}) =$	SPECTRAL DENSITY OF $\epsilon, \epsilon(z_1^{-1}, z_2^{-1})$	SPATIAL STRUCTURE	COMMENTS
1.	Causal, C1	$\frac{\partial^2}{\partial x \partial y} + a_1 \frac{\partial}{\partial x} + a_2 \frac{\partial}{\partial y} + a_3$	$(1 - \rho z_1^{-1}) \cdot (1 - \rho z_2^{-1})$	$(1 - \rho^2)^2 = \beta^2$		Hyperbolic Wave Equation
2.	Semicausal SC1	$\frac{\partial}{\partial y} - \frac{\partial^2}{\partial x^2} + a_1$	$(1 - \alpha z_1^{-1} - \alpha z_1^{-1} - \gamma z_2^{-1})$	β^2		Parabolic Diffusion Equation
3.	Semicausal SC2	$(\frac{\partial^2}{\partial x^2} + a_1) \cdot (\frac{\partial}{\partial y} + a_2)$	$1 - \alpha (1 - \rho z_2^{-1})(z_1 + z_1^{-1}) - \rho z_2^{-1}$	$(1 - \rho^2)^2 / (1 + \rho^2) \cdot [1 - \alpha (z_1 + z_1^{-1})]$		$\alpha = \rho / (1 + \rho^2)$ Covariance same as that of C1.
4.	Noncausal NC1	$\frac{\partial^2}{\partial x^2} + \frac{\partial^2}{\partial y^2} + a_1$	$1 - \alpha (z_1 + z_1^{-1} + z_2 + z_2^{-1})$	$\beta^2 [1 - \alpha (z_1 + z_1^{-1} + z_2 + z_2^{-1})]$		Poisson Equation
5.	Noncausal NC2	$(\frac{\partial^2}{\partial x^2} + \frac{\partial^2}{\partial y^2} + a_1)$	$[1 - \alpha (z_1 + z_1^{-1} + z_2 + z_2^{-1})]^2$	$\beta^2 [1 - \alpha (z_1 + z_1^{-1} + z_2 + z_2^{-1})]^2$		Biharmonic Equation
6.	Noncausal NC3	$(\frac{\partial^2}{\partial x^2} + a_1) (\frac{\partial^2}{\partial y^2} + a_2)$	$[1 - \alpha (z_1 + z_1^{-1})] \cdot [1 - \alpha (z_2 + z_2^{-1})]$	$\beta^2 [1 - \alpha (z_1 + z_1^{-1})] \cdot [1 - \alpha (z_2 + z_2^{-1})]$		$\beta^2 = (1 - \rho^2)^2 / (1 + \rho^2)^2$ Covariance same as C1

TABLE II

ACTUAL PARAMETERS MEASURED FOR THE 256x256 GIRL IMAGE TO MATCH THE 16x16 COVARIANCE MATRIX OF THE IMAGE TO THAT OF THE MODEL FOR VARIOUS MODELS.

S. NO.	MODEL	PARAMETERS
1.	Causal C1	$\rho = 0.962, \beta^2 = (1-\rho^2)^2 = 0.0055.$
2.	Semicausal SC1	$\alpha = 0.4275, \gamma = 0.1415, \beta^2 = 0.0198.$
3.	Semicausal SC2	$\rho = 0.962, \beta^2 = (1-\rho^2)^2 / (1+\rho^2) = 0.0029,$ $\alpha = \rho / (1+\rho^2).$
4.	Noncausal NC1	$\alpha = 0.2496, \alpha_1 = 0.95, \alpha, \beta^2 = 0.0744.$
5.	Noncausal NC2	$\alpha = 0.2494, \beta^2 = 0.0053.$
6.	Noncausal NC3	$\rho = 0.962, \beta^2 = (1-\rho^2)^2 / (1+\rho^2)^2 = 0.0015,$ $\alpha = \rho / (1+\rho^2).$

TABLE III

COMPARISON OF VARIOUS RESTORATION FILTERS IMPLEMENTED ON 65x65 BLOCKS OF DIFFERENT NOISY IMAGES FOR SIGNAL TO NOISE RATIO =1. THE ENTRIES SHOW THE IMPROVEMENT IN SIGNAL TO NOISE RATIO IN DECIBELS.

S. NO.	FILTERING MODEL	GIRL IMAGE	MOON IMAGE	COUPLE IMAGE	ERTS IMAGE
1.	Four Point Spatial Averaging	5.23 db	5.13 db	5.14 db	5.31 db
2.	Causal C1 Fourier-Weiner (F-W) Filter	9.12 db	7.20 db	8.10 db	8.42 db
		8.38 db	7.32 db	7.98 db	8.24 db
3.	Semicausal SC1 F-W Filter	9.46 db	8.89 db	9.30 db	9.64 db
		8.55 db	8.78 db	8.32 db	8.82 db
4.	Semicausal SC2 F-W Filter	8.87 db	6.61 db	8.27 db	8.54 db
		8.38 db	7.32 db	7.98 db	8.24 db
5.	Noncausal NC1 F-W Filter	10.05 db	8.75 db	8.70 db	9.88 db
		9.00 db	8.58 db	7.78 db	8.80 db
6.	Noncausal NC2 F-W Filter	9.48 db	8.05 db	8.04 db	9.32 db
		8.24 db	7.87 db	7.02 db	8.08 db
7.	Noncausal NC3 F-W Filter	8.92 db	6.59 db	8.31 db	8.46 db
		8.38 db	7.32 db	7.98 db	8.24 db

TABLE IV

COMPARISON OF VARIOUS IMAGE RESTORATION FILTERS IMPLEMENTED ON 65x65 BLOCKS OF DIFFERENT NOISY IMAGES FOR SIGNAL TO NOISE RATIO =2. THE ENTRIES SHOW THE IMPROVEMENT IN SIGNAL TO NOISE RATIO IN DECIBELS.

S. NO.	FILTERING MODEL	GIRL IMAGE	MOON IMAGE	COUPLE IMAGE	ERTS IMAGE
1.	Four Point Spatial Averaging	4.75 db	4.32 db	4.54 db	4.50 db
2.	Causal C1 Fourier-Weiner (F-W) Filter	5.23 db 4.59 db	3.00 db 3.01 db	4.36 db 4.34 db	3.92 db 3.62 db
3.	Semicausal SC1 F-W Filter	5.68 db 4.82 db	5.00 db 4.82 db	6.06 db 5.09 db	5.25 db 4.64 db
4.	Semicausal SC2 F-W Filter	5.01 db 4.59 db	2.51 db 3.01 db	4.44 db 4.34 db	3.88 db 3.62 db
5.	Concausal NC1 F-W Filter	6.64 db 5.79 db	5.29 db 5.15 db	5.54 db 4.71 db	5.85 db 5.05 db
6.	Noncausal NC2 F-W Filter	5.77 db 4.42 db	4.00 db 3.70 db	4.24 db 3.21 db	4.65 db 3.43 db
7.	Noncausal NC3 F-W Filter	5.02 db 4.59 db	2.49 db 3.01 db	4.44 db 4.34 db	3.82 db 3.62 db

TABLE V

COMPARISON OF VARIOUS IMAGE RESTORATION FILTERS IMPLEMENTED ON 65x65 BLOCKS OF DIFFERENT NOISY IMAGES FOR SIGNAL TO NOISE RATIO =5. THE ENTRIES SHOW THE IMPROVEMENT IN SIGNAL TO NOISE RATIO IN DECIBELS.

S. NO.	FILTERING MODEL	GIRL IMAGE	MOON IMAGE	COUPLE IMAGE	ERTS IMAGE
1.	Four Point Spatial Averaging	3.29 db	1.72 db	2.80 db	2.80 db
2.	Causal C1 Fourier-Weiner (F-W) Filter	0.91 db 0.49 db	-1.78 db -1.86 db	0.18 db 0.22 db	-0.96 db -1.22 db
3.	Semicausal SC1 F-W Filter	2.11 db 1.31 db	1.08 db 0.94 db	2.81 db 1.80 db	1.14 db 0.72 db
4.	Semicausal SC2 F-W Filter	0.78 db 0.49 db	-1.92 db -1.86 db	0.22 db 0.22 db	-1.04 db -1.22 db
5.	Noncausal NC1 F-W Filter	2.66 db 2.54 db	2.02 db 2.04 db	2.24 db 2.02 db	2.60 db 2.36 db
6.	Noncausal NC2 F-W Filter	2.06 db 0.56 db	-0.39 db -0.64 db	0.67 db -0.68 db	0.08 db -1.09 db
7.	Noncausal NC3 F-W Filter	0.79 db 0.49 db	-2.01 db -1.86 db	0.22 db 0.22 db	-1.02 db -1.22 db

APPENDIX II

1. AN OPERATOR FACTORIZATION METHOD FOR RESTORATION OF BLURRED IMAGES

A problem of restoration of images blurred by space invariant point spread functions (SIPSF) is considered. The SIPSF operator is factorized as a sum of two matrices. The first term is a polynomial of a noncirculant operator P and the second term is a Hankel matrix which affects only the boundary observations. The image covariance matrix is also factorized into two terms; the covariance of the first term is a polynomial in P and the second term depends on the boundary values of the image. Thus, by modifying the image matrix by its boundary terms and the observations by the boundary observations it is shown the Wiener filter equation is a function of the operator P , and can be solved exactly via the eigenvector expansion of P . The eigenvectors of the noncirculant matrix P are a set of orthonormal harmonic sinusoids called the Sine transform and the eigenvector expansion of the Wiener filter equation can be numerically achieved via a fast Sine transform algorithm which is related to the fast Fourier transform algorithm. The factorization therefore provides a fast Wiener restoration scheme for images and other random processes. Examples on 255 x 255 images are given.

KEY WORDS: Wiener Filtering, Karhunen Loeve Transform, Image Restoration, Image Processing

2. PARTIAL DIFFERENTIAL EQUATIONS AND FINITE DIFFERENCE METHODS IN IMAGE PROCESSING

PART II: IMAGE RESTORATION

Application of Partial Differential Equation (PDE) models for restoration of noisy images is considered. The hyperbolic, parabolic, and elliptic classes of PDEs yield recursive, semirecursive, and nonrecursive filtering algorithms. The two dimensional recursive filter is equivalent to solving two sets of filtering equations, one along the horizontal direction and other along the vertical direction. The semirecursive filter can be implemented by first transforming the image data along one of its dimensions, say column, and then recursive filtering along each row independently. The nonrecursive filter leads to Fourier domain Wiener filtering type transform domain algorithm. Comparisons of the different PDE model filters are made by implementing them on actual image data. Performances of these filters are also compared with Fourier Wiener filtering and spatial averaging methods. Performance bounds based on PDE model theory are calculated and implementation trade-offs of different algorithms are discussed.

KEY WORDS: Recursive Filtering, Two Dimensional Filtering, Kalman Filtering, Wiener Filtering, Image Restoration, Partial Differential Equations

3. FRAME TO FRAME RESTORATION OF DIFFUSION IMAGES

Frame to frame image data is acquired in many applications such as Radar, Biomedical, and Television imaging. In many situations, the imaging phenomenon can be modelled by a diffusion process. The sequence of image frames obtained may represent the observations of that process. Here, we consider the problem of recursive filtering of such images on a frame to frame basis. The major difficulties are computational because of three dimensional structure of the problem. In this paper a constant coefficient diffusion system is used for an interframe image restoration problem. Also, a two dimensional problem of restoration of blurred images can be solved by imbedding it in a three dimensional recursive filtering problem without blur. The model structure leads to a computationally feasible filtering algorithm achieving large reduction of dimensionality and is useful in real time hardware simulation of generation of such blurred image data as might occur in a forward looking radar (FLR).

KEY WORDS: Image Restoration, Distributed Parameter Systems, Recursive Filtering, Diffusion Equation, Image Simulation

4. FAST INVERSION OF BANDED TOEPLITZ MATRICES BY CIRCULAR DECOMPOSITION

Banded Toeplitz matrices of large size occur in many practical problems [1-6]. Here the problem of inversion as well as solving simultaneous equations of the type $Hx = y$, when H is a large banded Toeplitz matrix, is considered. It is shown via certain circular decompositions of H that such equations may be exactly solved in $O(N \log_2 N)$ rather than in $O(N^2)$ computations as in Levinson-Trench algorithms. Further, the algorithms of this paper are non-recursive (as compared to the Levinson-Trench algorithms) and afford parallel processor architectures and others such as transversal filters [17], where the computation time becomes proportional to N rather than $N \log N$. Finally, a principle of matrix decomposition for fast inversion of matrices is introduced as a generalization of the philosophy of this paper.

KEY WORDS: Toeplitz Matrix Inversion, Fast Matrix Inversion, Circulant Matrices